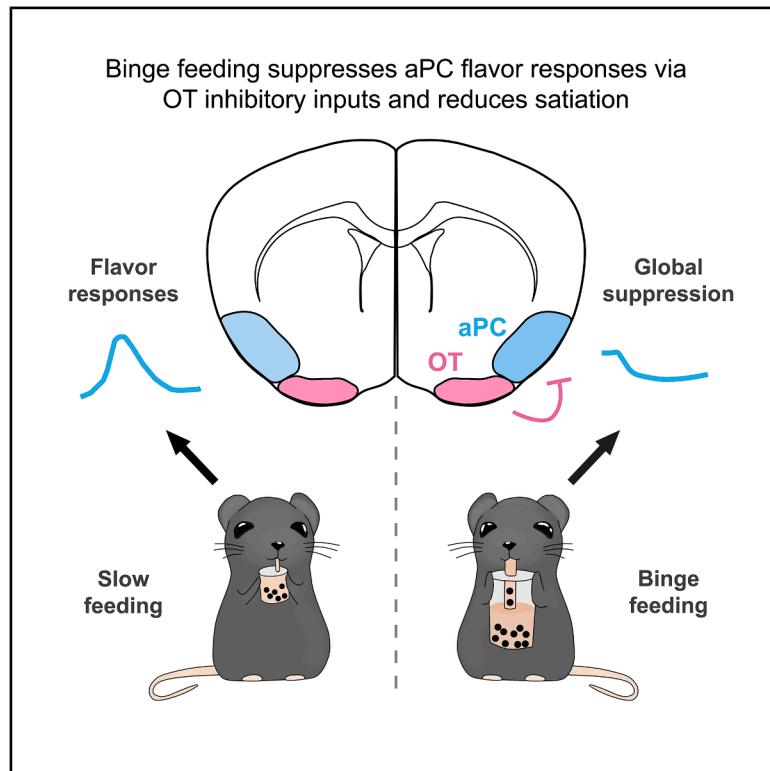


Feeding-induced olfactory cortex suppression reduces satiation

Graphical abstract



Authors

Hung Lo (羅鴻), Walter Cañedo Riedel, Malinda L.S. Tantirigama, ..., Wolfgang Kelsch, Dietmar Schmitz, Friedrich W. Jochenning

Correspondence

hung.lo@einsteinmed.edu (H.L.),
friedrich.jochenning@charite.de (F.W.J.)

In brief

Lo et al. show that binge feeding suppresses piriform (olfactory) cortex activity, reducing the brain's representation of food flavor. This suppression is driven by the olfactory tubercle and promotes continued eating by decreasing sensory satiation. The findings link sensory suppression to overeating and highlight a cortical mechanism regulating appetite.

Highlights

- Piriform (olfactory) cortex suppression scales with food value during binge feeding
- Feeding-induced suppression is driven by GABAergic input from the olfactory tubercle
- Suppression reduces flavor representation and correlates with reduced satiation
- Optogenetic piriform cortex inhibition increases food intake by prolonging feeding bouts

Article

Feeding-induced olfactory cortex suppression reduces satiation

Hung Lo (羅鴻),^{1,2,3,13,*} Walter Cañedo Riedel,^{4,5} Malinda L.S. Tantirigama,^{6,7} Anke Schoenherr,¹ Laura Moreno Velasquez,¹ Lukas Faiss,^{1,8} Amit Kumar,^{1,3} Aileen Hakus,^{1,3,8} Benjamin R. Rost,^{1,8} Matthew E. Larkum,⁶ Benjamin Judkewitz,^{1,2,7} Katharina Stumpfenhorst,⁹ Marion Rivalan,^{7,10} York Winter,⁹ Eleonora Russo,^{5,11} Wolfgang Kelsch,^{4,5} Dietmar Schmitz,^{1,2,3,7,8,12,14} and Friedrich W. Jochenning^{1,2,3,14,15,*}

¹Charité-Universitätsmedizin Berlin, Neuroscience Research Center, Charitéplatz 1, 10117 Berlin, Germany

²Charité-Universitätsmedizin Berlin, Einstein Center for Neurosciences Berlin, Charitéplatz 1, 10117 Berlin, Germany

³Charité-Universitätsmedizin Berlin, Institute of Cell and Neurobiology, 10117 Berlin, Germany

⁴Department of Psychiatry and Psychotherapy, Central Institute of Mental Health, Medical Faculty Mannheim, Heidelberg University, 68159 Mannheim, Germany

⁵Department of Psychiatry and Psychotherapy, University Medical Center, Johannes Gutenberg University, 55131 Mainz, Germany

⁶Humboldt Universität zu Berlin, Institut für Biologie, Charitéplatz 1, 10117 Berlin, Germany

⁷Charité-Universitätsmedizin Berlin, NeuroCure Cluster of Excellence, 10117 Berlin, Germany

⁸German Center for Neurodegenerative Diseases (DZNE) Berlin, Charitéplatz 1, 10117 Berlin, Germany

⁹Humboldt Universität zu Berlin, Cognitive Neurobiology, Philippstraße 13, 10115 Berlin, Germany

¹⁰Institute of Neuroscience Paris-Saclay, CNRS, University of Paris-Saclay, 91400 Saclay, France

¹¹The BioRobotics Institute, Department of Excellence in Robotics and AI, Scuola Superiore Sant'Anna, Piazza Martiri della Libertà, 33, 56127 Pisa, Italy

¹²Humboldt Universität zu Berlin, Bernstein Center for Computational Neuroscience, Philippstraße 13, 10115 Berlin, Germany

¹³Present address: Dominick P. Purpura Department of Neuroscience, Albert Einstein College of Medicine, Bronx, NY, USA

¹⁴Senior author

¹⁵Lead contact

*Correspondence: hung.lo@einsteinmed.edu (H.L.), friedrich.jochenning@charite.de (F.W.J.)

<https://doi.org/10.1016/j.neuron.2025.07.020>

SUMMARY

Binge feeding commonly leads to overeating. Experiencing flavor during food consumption contributes to satiation. Still, the interactions between flavor, binge feeding, and food intake remain unknown. Using miniscopes for *in vivo* calcium imaging in the anterior piriform cortex (aPC) in freely moving mice, we identified specific excitatory neuronal responses to different food flavors during slow feeding. Switching from slow feeding to binge feeding transformed these specific responses into an unspecific global suppression of neuronal activity. Consummatory aPC suppression scaled with food value. GABAergic neurons in the olfactory tubercle (OT) projected to the aPC and mirrored activity patterns in the aPC under different feeding conditions, consistent with transmitting a value signal. Closed-loop optogenetic manipulations demonstrated that suppressing the aPC during binge bouts reduces satiation by selectively prolonging feeding bouts. We propose that aPC suppression by the OT enhances food intake by reducing sensory satiation during binge feeding-associated states of high motivation.

INTRODUCTION

Satiation is an important feedback signal that reduces food consumption following food intake. Within the framework of the three canonical phases of feeding behavior (seeking, consumption, and satiety),¹ the mechanisms that diminish satiation during consumption of high hedonic value food in the absence of metabolic need remain poorly understood.² Eating rapidly over a short period, commonly known as binge eating, reduces satiation.^{3–8} An increased eating rate is often linked to overeating beyond metabolic needs⁹ and obesity,¹⁰ while

lowering the eating rate can effectively mitigate food consumption.^{11,12}

The canonical explanation for the reduction of satiation due to binge feeding compared with slow feeding is based on the delayed transfer of homeostatic signals from the gastrointestinal tract to the brain.^{13–15} Although it is undisputed that visceral satiation results from ingestion and absorption, there is also sensory satiation mediated by flavor representation.^{16–20} Experiments using gastric tubes have demonstrated sensory satiation by bypassing the sensory experiences of food within the oral cavity through direct infusion. Oral bypassing reduces satiety and

accelerates gastric emptying compared with regular feeding in humans and rodents.^{18,21,22} Recent studies have uncovered hypothalamic and brainstem circuits that mediate sensory satiation.^{23,24} However, it remains unclear how sensory representation at the cortical level connects to satiation and how sensory satiation is associated with the hedonic value and palatability of food.

During consumption, the sensory representation of food is primarily mediated by flavor. Flavor is a multisensory phenomenon involving multiple interconnected cortical areas, including the primary olfactory cortex, or piriform cortex (PC), which represents smell; the gustatory cortex (GC), representing taste; and, to some degree, other sensory cortices for the tactile and visual aspects of food.^{25,26} The PC typically represents odor identity using a concentration-invariant population code of activated neurons.^{27,28} Activating populations in the PC is sufficient to elicit conditioned appetitive and aversive behavioral responses.²⁹ Despite its essential contribution to flavor experience, the role of olfactory flavor representation in the PC during the consumption phase of feeding remains poorly understood.^{30,31}

RESULTS

Flavor representation in the anterior piriform cortex is modulated by feeding rate

We established a self-paced feeding paradigm combined with calcium (Ca^{2+}) imaging in freely moving mice to examine how the feeding rate affects sensory representation. We built a liquid food (Ensure, an energy-dense flavored nutrient solution) delivery system that feeds mice at two different rates to induce slow or binge feeding experimentally (Figure 1A). Mice consumed more liquid food and licked at a higher rate (Figures S1E–S1H) during binge feeding, indicating the attribution of greater value, due to a greater rate of reward, to binge feeding.³²

We imaged Ca^{2+} transients of excitatory anterior olfactory (piriform) cortex (aPC) neurons expressing GCaMP6f (Figures 1B and S1I–S1K) using a miniscope to record neuronal activity in freely moving mice. When comparing periconsummatory neuronal activity during slow and binge feeding, binge feeding bouts demonstrated a switch toward robust global suppression (Figure 1C; Video S1). For categorization, we analyzed neuronal responses during slow feeding, as this feeding mode provided a larger number of clearly separated individual trials. We used interleaved water deliveries to classify neurons into food-specific, water-specific, non-selective, and non-responding categories during slow feeding (Figures 1D, 1E, S2A, and S2B).

Using different Ensure flavors and sucrose, we found that aPC neurons exhibit distinct, mostly non-overlapping responses to different flavors (Figures 1F and 1G). We conclude that the aPC differentially represents different flavors, including smell and taste stimuli. The proportion of cells in the flavor-specific subclasses during slow feeding is comparable to the odor-specific populations observed in the aPC.^{33,34} For simplicity, we refer to the subpopulation of neurons activated by Ensure and not by water as food-activated neurons.

The classification during slow feeding permitted us to test whether the observed global suppression during binge feeding extended to the subpopulation of food-activated neurons. If we

observed a preservation of the activity in food-activated neurons, then global suppression would be a classical lateral inhibition phenomenon. Binge-induced suppression extended to all neuron classes (food-activated, water activated, and non-responding) except non-selective (consumption-activated) ones, arguing against classical lateral inhibition (Figures 1H, 1I, and S2D–S2H).

Activity in the PC represents odor identity through a distributed population code.^{33,35–39} Our results during slow feeding are compatible with a similar model for peri-consummatory flavor representation in the aPC. When orthonasally sniffed odors are presented at different intensities, the distributed population code and the neuronal firing rates remain similar.³⁸ During binge feeding, the sensory stimulation from the same flavor increases due to the higher food volume. Based on the aforementioned results on orthonasal sniffing of odors, we did not expect the changes in the population representation of flavors that we indeed observed during binge feeding (Figures 1H, 1I, and 2E). Thus, our data point to a feeding rate-dependent modulation of flavor representation in the aPC during food consumption that fundamentally alters the flavor-specific population code and differs from the representation of orthonasally presented odors during sniffing.

Flavor representation in the GC is stable across feeding rates

Global neuronal suppression in the aPC induced by binge feeding may be a more general phenomenon also observed in other brain regions representing flavor. To test this hypothesis, we performed Ca^{2+} imaging in the GC (GC, granular, and dysgranular insular cortex) using a miniscope (Figure S1K) and tracked taste representation during slow and binge feeding (Figures 2A–2C and S3A–S3G). Again, we focused on the subpopulation of food-activated neurons identified during slow feeding. In contrast to aPC, food-activated GC neurons maintained activity during binge feeding, with prolonged responses reflecting increased orosensory exposure (Figures 2D–2H). In addition, we did not find significant suppression of activity in the general population of GC during binge feeding compared with slow feeding (Figures 2D, 2E, S3H, and S3I).

We compared single-cell activity in food-activated neurons across feeding rates. In the GC, responses during slow and binge feeding were linearly correlated, while no such correlation was observed in the aPC, indicating non-uniform, general inhibition during binge feeding (Figure 2F).⁴⁰ Cumulative distributions of $\Delta(\text{binge-slow})$ Z-scored Ca^{2+} signals further confirmed that GC neurons showed smaller net reductions and more frequent increases than aPC neurons (Figure 2G), consistent with preserved flavor representation in the GC during binge feeding (Figure 2H).

Binge feeding-induced aPC suppression is not inherited from the olfactory bulb

Next, we wanted to understand possible mechanisms underlying binge feeding-induced generalized suppression in the aPC. The aPC is the first cortical relay of the olfactory system and receives direct sensory afferent inputs from the olfactory bulb (OB).⁴¹ We tested whether a reduction in sensory input from the OB could

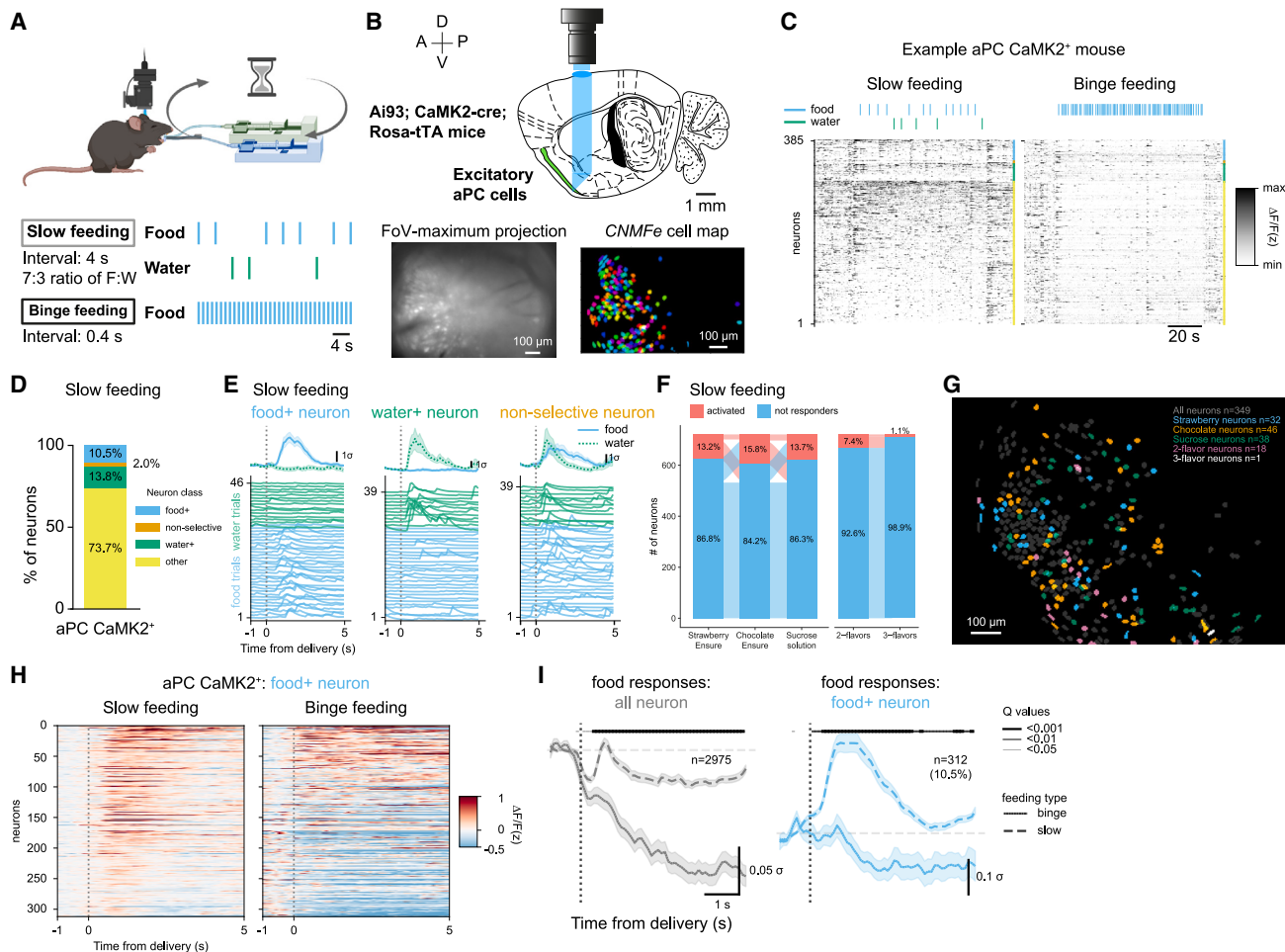


Figure 1. Feeding rate modulates flavor representations in aPC

(A) Miniscope recording and behavioral protocol for slow feeding and binge feeding.
 (B) Top: schematics of gradient-index (GRIN) lens/prism (blue shade) implantation in aPC (green structure). Bottom: field of view (FoV) of miniscope recordings and extracted cell maps by constrained non-negative matrix factorization (CNMFe).
 (C) Example Ca^{2+} traces of aPC neurons during slow feeding and binge feeding from one mouse. Neurons are sorted by response type during slow feeding, as colored in (D).
 (D) Percentage of aPC neurons activated during slow feeding by food, water, or non-selective consumption vs. non-responding neurons ($n = 2,975$ cells, 481 slow feeding trials, and 241 binge feeding trials in 8 mice).
 (E) Trial-averaged and single-trial responses of example aPC food-activated, water-activated, and non-selective neurons upon slow feeding.
 (F) Percentage of aPC neurons activated by different flavors of Ensure and sucrose solution during slow feeding.
 (G) Cell map of activated aPC neurons of different flavors during slow feeding.
 (H) Trial-averaged responses to food deliveries of individual aPC CaMK2^+ food-activated neurons upon slow feeding and binge feeding ($n = 312$ cells in 8 mice).
 (I) Trial-averaged responses of the general population and food-activated aPC CaMK2^+ neurons upon slow and binge feeding (n is the same as in D and H, respectively). Dashed vertical line indicates start of the food delivery. Shaded line above denotes the adjusted p values (q values) of each time point, different line widths represent different values (from thin to thick: $q < 0.05$, $q < 0.01$, $q < 0.001$). For (E) and (I), data are shown as mean \pm SEM.

explain global suppression during binge feeding in the aPC. To this end, we performed *in vivo* head-fixed three-photon Ca^{2+} imaging of OB mitral cells during slow and binge feeding. Mitral cells are the major neuronal population that propagates odor information to higher olfactory cortices, including the aPC.²⁷ In contrast to the aPC, OB mitral cells remained activated upon binge feeding (Figures 3A–3D, S4A, and S4B). We further performed nasal lavage with 0.5% Triton solution to induce temporary hyposmia by ablation of olfactory sensory neurons (OSNs) in

mice⁴² (Figures S4C and S4D; hyposmia verified by a buried food test). Our procedure caused a 30% drop in active aPC neurons in the field of view detected with Ca^{2+} imaging, consistent with reduced olfactory inputs to the aPC (Figure S4E). Both intact net excitatory OB output during slow and binge feeding and preserved suppression in hyposmic mice showing a 30% drop in detected aPC neurons suggest that aPC suppression is not inherited from peripheral olfactory pathways (Figures 3 and S4).

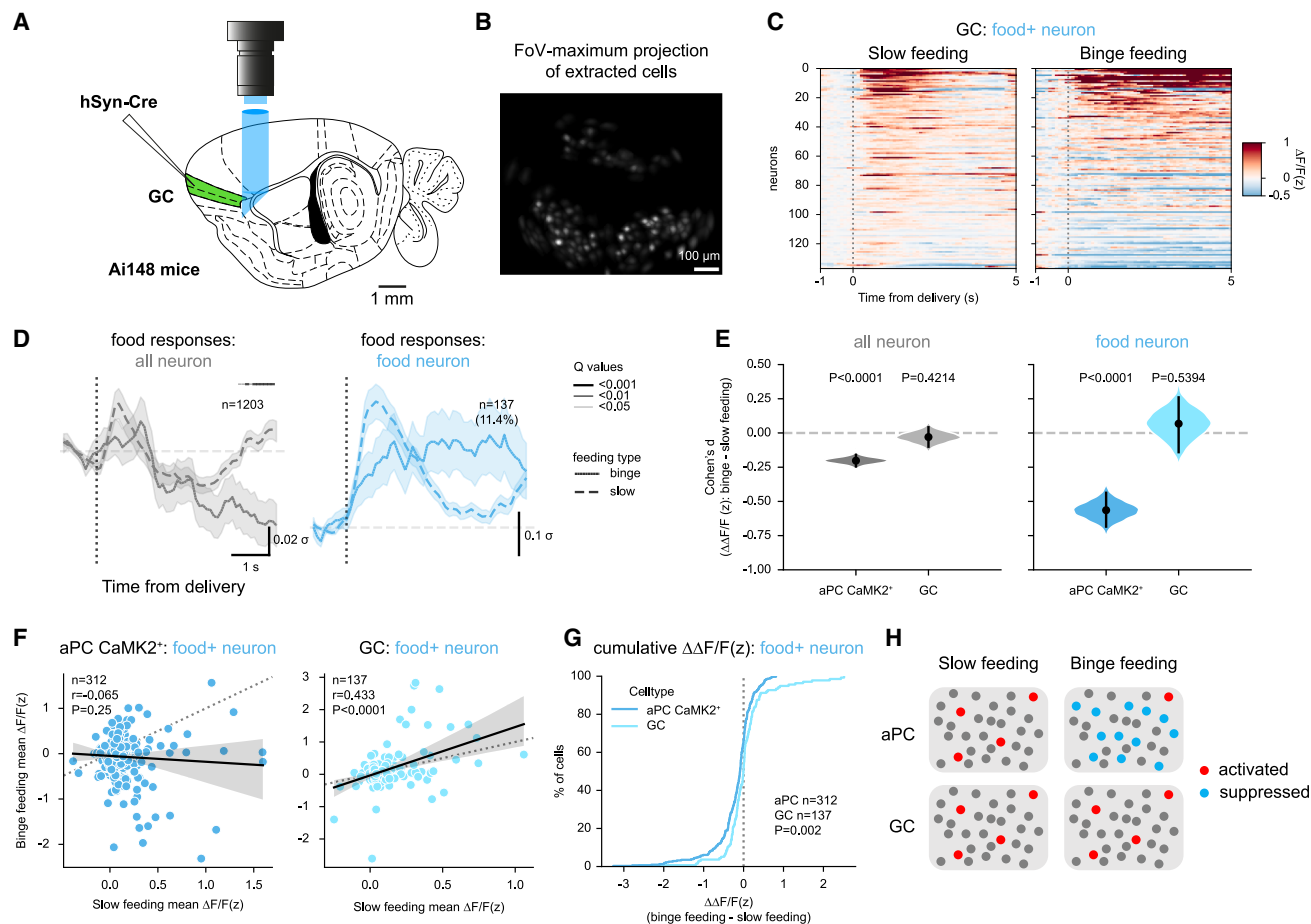


Figure 2. Flavour representation in the GC is stable across feeding rates

(A) Schematics of GRIN lens/prism implantation in the GC.
 (B) Cell maps extracted by CNMFe.
 (C) Trial-averaged responses of individual GC food-activated neurons upon slow and binge feeding ($n = 137$ from 3 mice).
 (D) Trial-averaged responses of the population and the food-activated GC neurons upon slow and binge feeding ($n = 1,203$ cells from 3 mice). Shaded line above denotes the adjusted p values (q values) of each time point, different line widths represent different values (from thin to thick: $q < 0.05$, $q < 0.01$, $q < 0.001$).
 (E) Estimated effect size (Cohen's d) of binge feeding-induced modulation in aPC CaMK2⁺ and GC neurons, all neurons, and food-activated subclass. p values calculated with permutation test (5,000 times bootstrapping; n is the same as in D).
 (F) Cell-wise comparison of neuronal responses upon slow and binge feeding in food-activated aPC CaMK2⁺ and GC neurons (n is the same as in Figures 1C and 1F).
 (G) Cumulative distribution of the difference (binge feeding vs. slow feeding) of Z-scored $\Delta F/F(z)$ ($\Delta \Delta F/F(z)$) in food-activated aPC CaMK2⁺ and GC neurons (n is the same as in F).
 (H) Schematics of neuronal responses in the aPC and the GC during slow feeding and binge feeding.
 For (F), r and p represent the correlation coefficient and p value of Pearson's r . For (D), data are shown as mean \pm SEM. For (E), data are shown as means of bootstrapped effect sizes (Cohen's d) \pm 95% confidence interval. For (G), the p value is calculated from the Kolmogorov-Smirnov test.

Binge feeding-induced aPC suppression extends to the major classes of local GABAergic neurons

Because the feeding rate leaves the excitatory sensory drive unaffected, enhanced recruitment of inhibitory interneurons during binge feeding could mediate the global suppression of the aPC. Local inhibitory feedback interneurons—activated by recurrent excitatory activity—predominantly inhibit odor responses in the aPC, while the contribution to global inhibition from feedforward interneurons is minor.²⁸ Thus, we probed the activity levels of aPC parvalbumin-positive (PV⁺) and somatostatin-positive (SST⁺) inhibitory interneurons during slow

and binge feeding, as they comprise a large proportion of local feedback circuits.⁴³ However, both PV⁺ and SST⁺ interneurons display strong suppression during binge feeding, in contrast to the significantly smaller suppression observed during slow feeding (Figures 3E–3L). Similar to the excitatory neurons, we identified a subpopulation of food-activated interneurons during slow feeding (Figures S4H, S4I, S4K, and S4L). These food-activated interneurons also exhibited significant global suppression during binge feeding (Figures S4J, S4M, and S4N). Therefore, changes in the excitation-to-inhibition ratio of sensory afferent and local recurrent aPC circuits do not

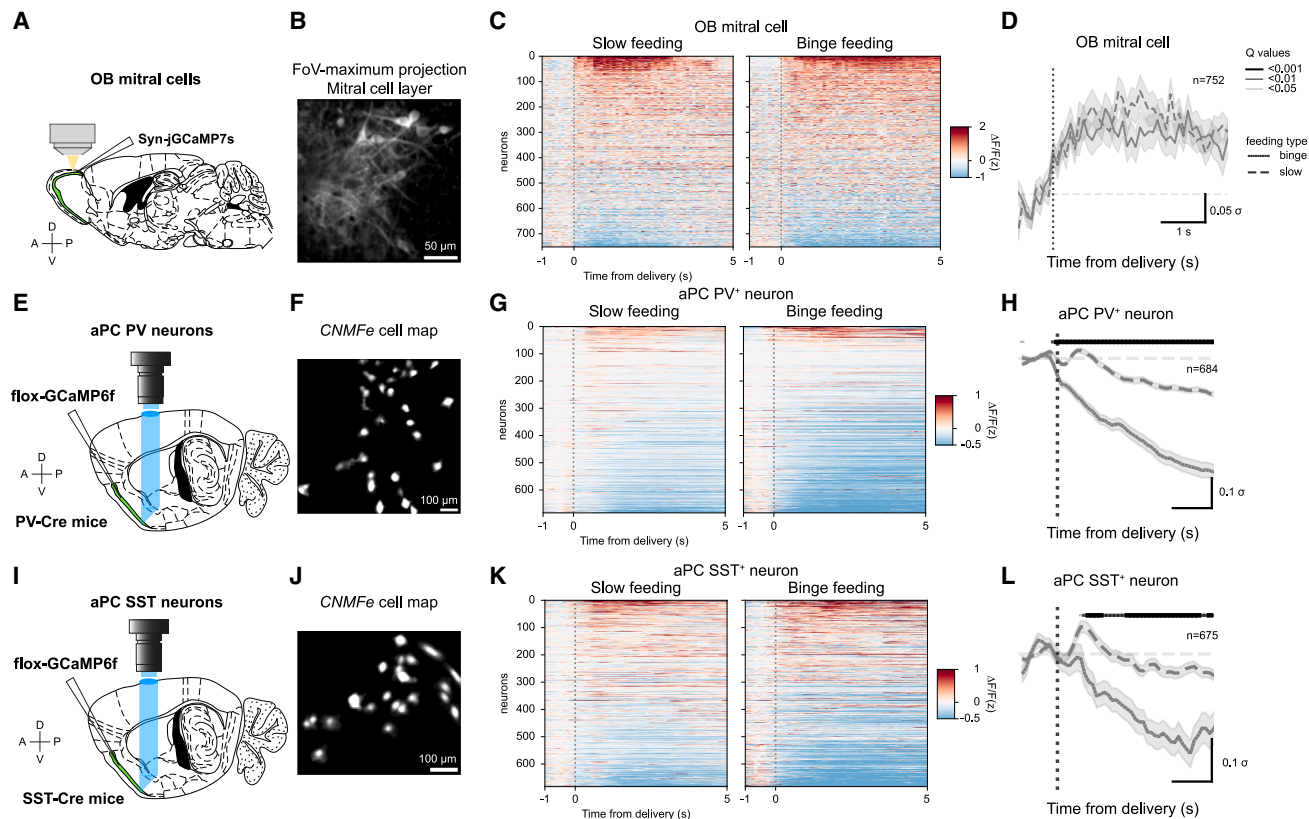


Figure 3. Binge feeding-induced aPC suppression is not inherited from the OB and extends to GABAergic aPC neurons

- (A) Schematics of 3P- Ca^{2+} imaging in OB mitral cells.
 (B) FoV of OB mitral cells.
 (C) Trial-average of individual OB mitral cells upon slow and binge feeding ($n = 752$ cells from 4 mice).
 (D) Trial-average of OB mitral cell population responses upon slow and binge feeding (n is the same as in C).
 (E) Schematics of Ca^{2+} imaging in aPC PV⁺ neurons.
 (F) Cell map of aPC PV⁺ neurons extracted by CNMFe.
 (G) Trial-average of individual aPC PV⁺ neurons upon slow and binge feeding ($n = 684$ cells from 3 mice).
 (H) Trial-average of population aPC PV⁺ neuron responses upon slow and binge feeding (n is the same as in G).
 (I) Schematics of Ca^{2+} imaging in aPC SST⁺ neurons.
 (J) Cell map of aPC SST⁺ neurons extracted by CNMFe.
 (K) Trial-average of individual aPC SST⁺ neurons upon slow and binge feeding ($n = 675$ cells from 3 mice).
 (L) Trial-average of population aPC SST⁺ neuron responses upon slow and binge feeding (n is the same as in K).

For (D), (H), and (L), data are shown as mean \pm SEM, and the shaded line above denotes the adjusted p values (q values) of each time point, with different line widths representing different values (from thin to thick: $q < 0.05$, $q < 0.01$, $q < 0.001$).

appear to mediate the global suppression of aPC activity during binge feeding.

GABAergic neurons in the OT project to the aPC and are functionally connected with the aPC

Our results on OB mitral cells (Figure 3), OSN ablation (Figure S4), and GABAergic aPC neurons (Figures 3 and S4) suggest that the binge feeding-induced suppression originates outside the aPC, either via long-range GABAergic inputs or through neuromodulatory systems. We, therefore, searched for an inhibitory input to the aPC that is activated by feeding and exhibits stronger activation from binge feeding than from slow feeding.

Serotonin projections from the dorsal raphe to the aPC are quite prominent.⁴⁴ Furthermore, serotonergic neurons in the dor-

sal raphe are activated during feeding⁴⁵ and decrease activity in the aPC *in vivo*.⁴⁶ With respect to dopaminergic modulation, patch-clamp experiments in acute aPC brain slices demonstrated a net inhibitory effect of dopamine on aPC neurons (Figures S5E–S5G). Serotonin and dopamine levels in the aPC show similar decreases during slow and binge feeding and could therefore be excluded as drivers of suppression (Figure S5).

Binge feeding is more valuable to the animal than slow feeding (see also Figure S1). Therefore, we next looked for inhibitory olfactory-related structures outside the aPC that could relay this value signal to the aPC but not to the GC during binge feeding. The olfactory tubercle (OT) is a ventral striatal structure located on the medial side of the aPC and activated by rewards and odors.⁴⁷ The OT is also involved in odor-cue-associated reward learning,⁴⁸ encoding odor valence.^{49,50}

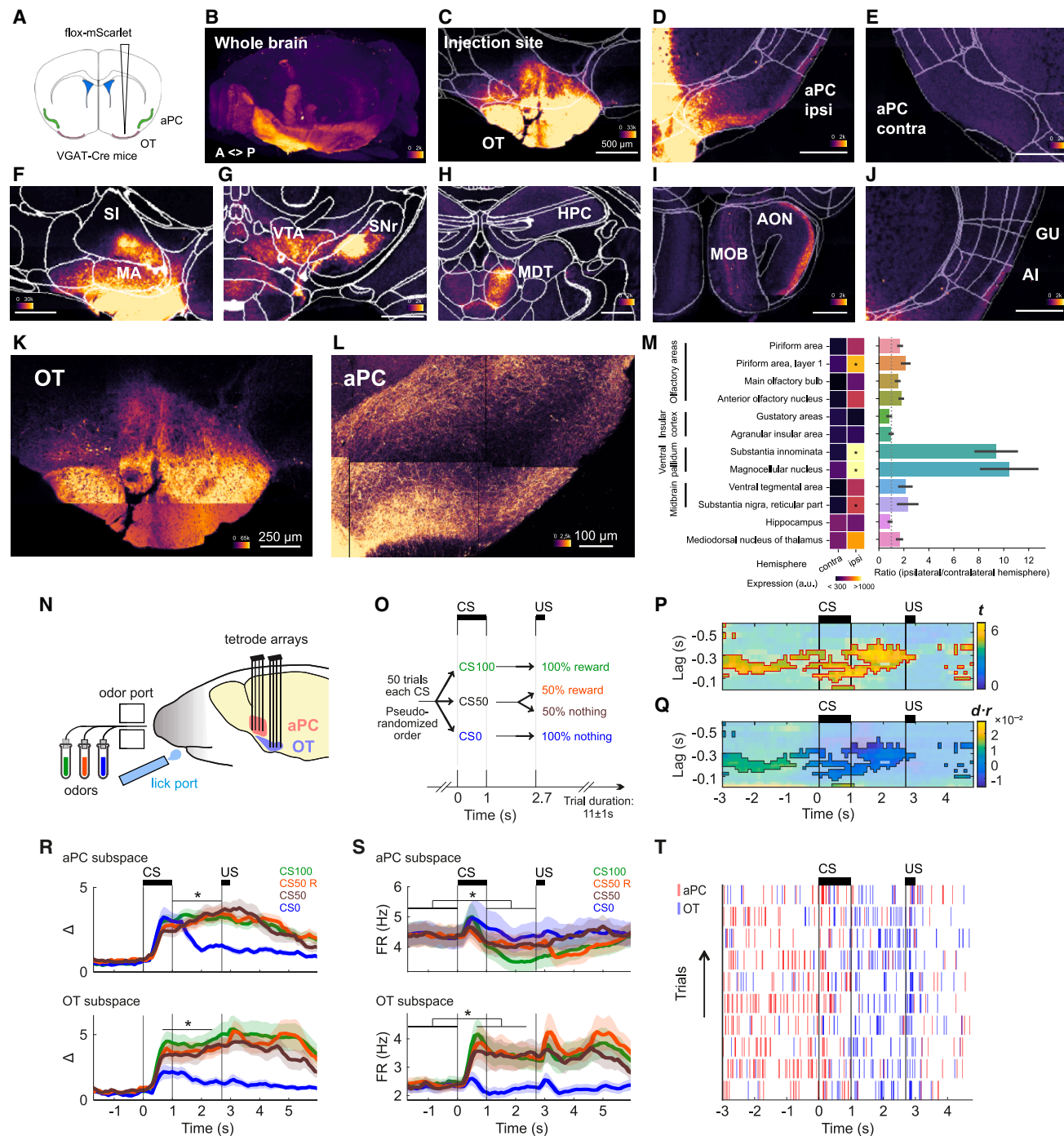


Figure 4. GABAergic neurons in the OT functionally project to the aPC

(A) Schematics of mapping axonal projection of OT VGAT⁺ neurons.

(B) Whole brain axonal projection pattern. Image is reconstructed from serial two-photon tomography.

(C–L) Viral expression and axonal projections in different brain regions; OT (C), aPC ipsilateral side (D) and contralateral side (E), VP (F), midbrain (G), dorsal thalamus and HPC (H), AON and MOB (I), insular cortex (including GC, J), and high-resolution zoomed-in image of viral injection site in OT (K) and aPC (L).

(M) Left: axonal expression intensity in different brain regions, permutation test of 10,000 resamples was used for comparison of expression in ipsilateral and contralateral hemispheres. Right: ratio of intensity in different hemispheres. OT, olfactory tubercle; aPC, anterior piriform cortex; MA, magnocellular nucleus; SI, substantia innominata; VTA, ventral tegmental area; SNr, substantia nigra, reticular part; HPC, hippocampus; MDT, mediadorsal nucleus of thalamus; AON, anterior olfactory nucleus; MOB, main olfactory bulb; GU, gustatory areas; AI, agranular insular area.

(N) Mice were implanted with dual-site tetrode arrays for simultaneous recordings in aPC and OT in a head-fixed configuration.

(legend continued on next page)

To test whether GABAergic neurons in the OT project to the aPC, we performed anterograde labeling in the OT vesicular GABA transporter (VGAT)⁺ neurons and mapped the axonal projections. We found OT VGAT⁺ neurons project unilaterally to layers 1 and 3 of PC, in both the anterior and posterior regions. In contrast, the cell bodies in PC layer 2 were spared (Figures 4A–4E, 4L, and 4M). In addition to the PC projection, we also observed projections to the mediodorsal thalamus (MDT, Figures 4H and 4M) and the anterior olfactory nucleus (AON, Figures 4I and 4M). We did not find significant projections to the GC (Figures 4J and 4M). In keeping with previous work on D1R- and D2R-expressing GABAergic neurons in the OT, we found comparatively stronger projections to the ventral pallidum (VP)⁵¹ (Figures 4F and 4M). Considering that the anterior part of the VP constitutes a reward-driven GABAergic cell population adjacent to the OT, two axonal tracing studies in the VP did not find projections to the aPC,^{52,53} supporting that our axonal tracing results are likely not contaminated by GABAergic neurons in the VP.

In addition to anatomically characterizing inhibitory connections between the OT and the aPC, we also tested *in vivo* for functional connectivity compatible with an excitation-inhibition sequence from the OT to the aPC. We reanalyzed a previously published dataset of mice implanted with an anatomically shaped dual-site tetrode array in the OT and the aPC (Figure 4N).⁴⁸ In a head-fixed configuration, mice were trained in a delay-conditioned task (Figure 4O).

We probed lagged interactions between the two regions with canonical correlation analysis (CCA; see STAR Methods).^{54,55} We observed functional interactions in both aPC→OT and OT→aPC directions during the inter-trial interval (Figures 4P and S6C). The aPC→OT functional interaction ceases after the conditioned stimulus (CS; Figure S6C). The OT→aPC functional interaction, however, reaches a maximum later during the delay prior to reward, with a lag between OT and aPC of about 300 ms (Figure 4P). After CS onset, the weights defining the subspaces of the two regions are in average of opposite sign (Figure 4Q), consistent with an excitation-inhibition interaction. Activity in the functional interaction subspace is more strongly modulated for trials with reward-predicting CS (CS100 and CS50) than for the non-rewarded one (CS0) (Figure 4R). For trials with reward-predicting CS, the units modulated by the communication sub-

space are excited in OT and inhibited in aPC (Figures 4S and 4T). The fact that 37 out of 67 sessions showed significant interactions with the limited number of units recorded in each region (Figure S6B) suggests that units in both regions broadly participated in the interaction. From the anatomically characterized inhibitory connections between the OT and aPC and from the corresponding *in vivo* functional connectivity, we conclude that the OT suppresses the aPC as a function of the anticipated reward outcome.

GABAergic OT neurons mirror neuronal dynamics in the aPC during feeding in different motivational states

Our anatomical and functional connectivity data suggest that the activity of GABAergic neurons in the OT inhibits the aPC (Figure 5). Next, we tested whether GABAergic neurons in the OT are activated during feeding and mirror the global suppression pattern in the aPC during this process. Using *in vivo* miniscope Ca²⁺ imaging of OT VGAT⁺ neurons (Figures 5A and S6), we found that a subset of OT VGAT⁺ neurons was activated during slow feeding (31.7%, $n = 236/744$, Figures 5B and 5C). These feeding-activated OT neurons were more strongly activated by binge feeding and remained active throughout the binge feeding bouts (Figures 5B and 5C). The neuronal dynamics of the OT VGAT⁺ neurons during binge and slow feeding mirror the dynamics of aPC neurons, further suggesting that the OT may drive the binge feeding-induced aPC suppression.

In the OT→aPC communication subspace, we observed a response modulation by value (Figure 4R). We, therefore, wanted to test whether the activation of the OT and the subsequent suppression in the aPC scaled with the reward magnitude of our food stimulus. We tested this hypothesis by altering the palatability of the food by diluting the Ensure to 25% of the original concentration.^{2,56} When mice consumed the less palatable, diluted Ensure, the binge feeding-induced aPC suppression was reduced (Figures 5D, 5E, and 5J). The binge-activated OT VGAT⁺ neurons also showed lower activation during consumption of diluted Ensure, further suggesting a link between OT and aPC under conditions of different palatability (Figures 5F and 5J).

Metabolic states like hunger and satiety profoundly affect sensory systems.^{57–61} Consequently, we wondered whether

(O) Three odors (conditioned stimulus [CS]) associated with water reward-outcome (unconditioned stimulus [US]) probabilities of 0%, 50%, and 100%, respectively, were presented in pseudorandomized order.

(P) Significance of the canonical correlation r along the first pair of canonical components. Color map displays t -statistics obtained from an LME estimating the Z score of r against the shuffle distribution in the cohort. Color map shows OT to aPC interactions, between the aPC activity (at the time reported on the x axis), and the activity of OT measured at various preceding time points (y axis). Solid bins indicate statistical significance ($p < 0.05$ after Bonferroni correction).

(Q) Direction of the correlation $d \cdot r$. Negative values indicate mean projection weights of the two regions on the first canonical dimension have opposite signs. Mean across sessions ($n_{\text{sessions}} = 67$), shaded by significance from (P).

(R) Absolute deviation from baseline (mean \pm SEM) along the first canonical components of aPC (top) and OT (bottom). Canonical components computed in the window of peak CCA significance, reached during the delay (only significant sessions included, $n_{\text{sessions}} = 37$). The deviation from baseline in the interaction subspace is smaller for CS0 compared with CS100 and CS50 (LME with post hoc comparison: for aPC, CS100 vs. CS0, $t(108) = 3.8$, $p = 2.0 \times 10^{-4}$, CS50 vs. CS0, $t(108) = 3.1$, $p = 2.4 \times 10^{-3}$ and for OT, CS100 vs. CS0, $t(108) = 4.7$, $p = 7.5 \times 10^{-6}$, CS50 vs. CS0, $t(108) = 3.3$, $p = 1.3 \times 10^{-3}$).

(S) Firing rate modulation (mean \pm SEM) along the canonical components from (Q). In contrast to (Q), the associated firing rate is obtained as a weighted mean of unit rates weighted with the absolute value of the CCA weights, thereby preserving the sign of modulation in each region in terms of excitation and inhibition. The communication subspace corresponds to an inhibition of the aPC for reward-predicting stimuli (CS100 and CS50) (LME: $\beta = -0.56$ Hz, $t(3699) = -2.0$, $p = 0.048$) and excitation of the OT (LME: $\beta = 0.86$ Hz, $t(3699) = 2.0$, $p = 0.044$).

(T) Spiking activity during the last ten CS100 trials of an example session shown for the two highest absolute-weighted units identified by CCA. The units have weights with opposite signs.

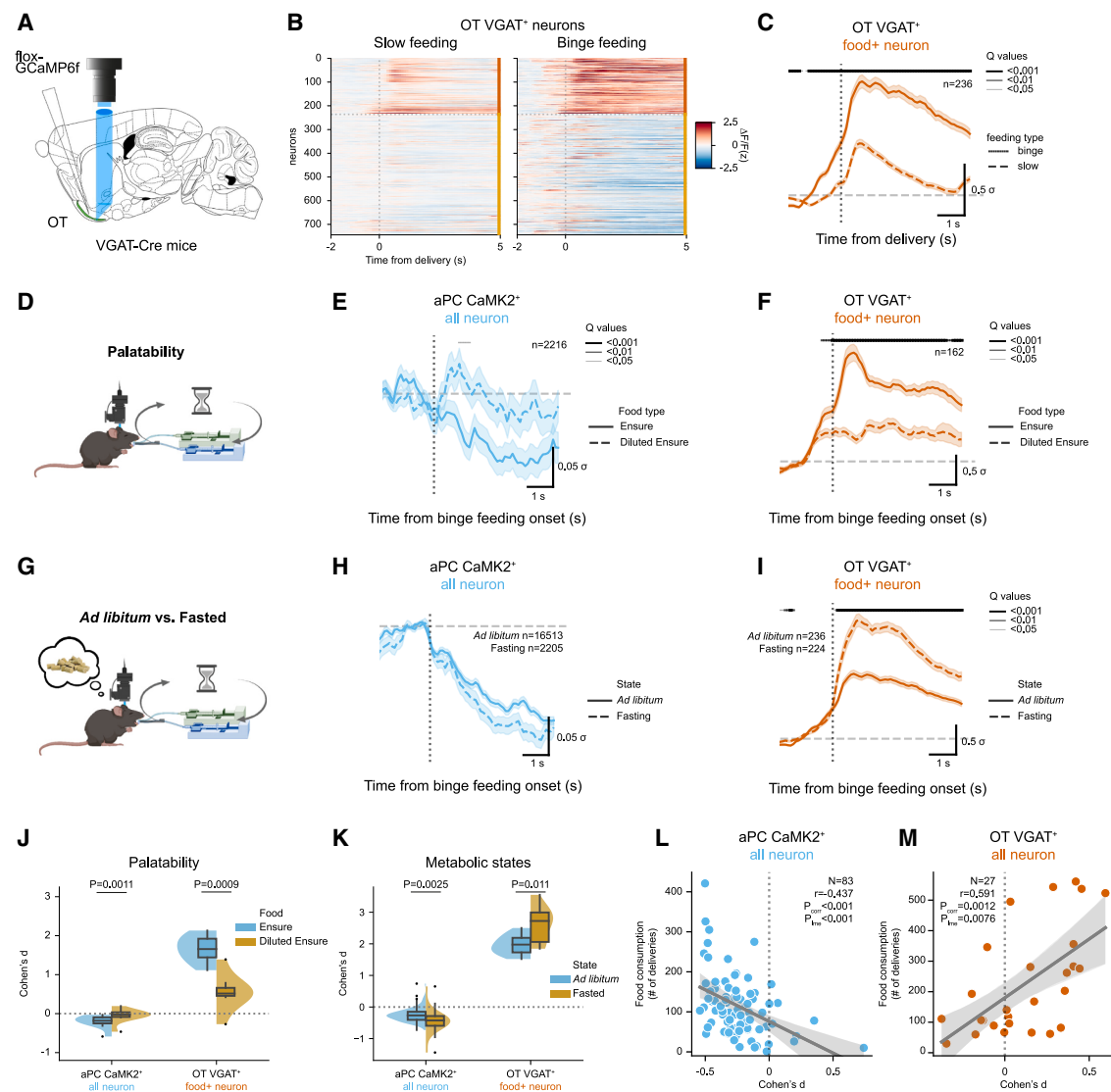


Figure 5. OT GABAergic neurons mirror neuronal dynamics in the aPC during feeding

- (A) Schematics of Ca^{2+} imaging in OT VGAT⁺ neurons.
 (B) Trial-average response of individual OT VGAT⁺ neurons to food (Ensure) upon slow and binge feeding. Neurons are sorted by different feeding response types by time series clustering ($n = 745$ cells from 3 mice).
 (C) Trial-average response of OT VGAT⁺ food-activating neurons upon slow and binge feeding ($n = 236$ cells from 3 mice).
 (D) Schematics of palatability testing paradigm.
 (E) Trial-average response of population aPC CaMK2⁺ neurons to Ensure and 5-fold diluted Ensure during binge feeding ($n = 2,216$ cells from 3 mice).
 (F) Trial-average response of food-activating OT VGAT⁺ neurons to Ensure and 5-fold diluted Ensure during binge feeding ($n = 162$ cells in 3 mice).
 (G) Schematics of fasting paradigm.
 (H) Trial-average response of population aPC CaMK2⁺ neurons to Ensure during binge feeding upon *ad libitum* or overnight fasting (*ad libitum* $n = 16,513$ cells from 8 mice, fasting $n = 2,205$ from 8 mice).
 (I) Trial-average response of food-activating OT VGAT⁺ neurons during binge feeding upon *ad libitum* or overnight fasting (*ad libitum* $n = 236$ cells from 3 mice, fasting $n = 224$ from 3 mice).
 (J) Estimated binge feeding modulation upon different palatability (n is the same as in E and F).
 (K) Estimated binge feeding modulation upon different metabolic states (n is the same as in H and I).
 (L and M) Correlations between session-specific food intake and modulation of neuronal activity in aPC CaMK2⁺ neurons upon binge feeding ($n = 83$ from 8 mice, M) or in OT VGAT⁺ neurons ($n = 27$ sessions from 3 mice, L).

For (C), (E), (F), (H), and (I), data are shown as mean \pm SEM, and the shaded line above denotes the adjusted p values (q values) of each time point, with different line widths representing different values (from thin to thick: $q < 0.05$, $q < 0.01$, $q < 0.001$). For boxplot in (J) and (K), the center line shows the median, the box limits show the quartiles, the whiskers show $1.5 \times$ the interquartile range, and the points show the outliers. For (J) and (K), p values were calculated with the unpaired t test. For (L) and (M), p values were calculated with the Pearson's correlation coefficient.

increasing the caloric need impacted the consumption-correlated suppression of aPC neuronal activity during binge feeding. Compared with *ad libitum*-fed conditions, global binge feeding-induced suppression of aPC neuronal activity was greater in fasted mice (Figures 5G, 5H, and 5K). As expected, feeding-activated inhibitory neurons in the OT showed stronger activation after overnight fasting (Figures 5I and 5K). This indicates that aPC inhibition and OT activation also scale with metabolic state.

For a broader understanding of the interaction between metabolic state and flavor representation, we also examined the effect of fasting on GC activity. In GC, we also observed increased suppression during binge feeding in the fasted condition compared with the *ad libitum*-fed condition (Figure S6G). This contrasts with the generally low level of GC suppression during binge feeding (Figures 2D–2F). We conclude that suppression of flavor representation extends to the GC under conditions of caloric need. In *ad libitum* conditions, where palatability significantly impacts food intake, binge feeding-associated suppression of neuronal activity is limited to the olfactory component of flavor representation.

Binge feeding-induced aPC suppression predicts reduced satiation

Flavor representation of food items contributes to satiation, and bypassing flavor representation via an intragastric catheter reduces satiation and accelerates gastric emptying of identical food items.^{18,20} Accordingly, we hypothesize that the global aPC suppression during binge feeding constitutes a mechanistic link between the cortical flavor response and decreased satiation. Under *ad libitum* feeding conditions, mice consumed different amounts of food on different experimental days, which we take as a proxy for differences in satiation. This noticeable behavioral variability in our recording sessions correlates with temporal progression, suggesting that binge feeding gradually escalates over time (Figure S6F). We, therefore, investigated whether this behavioral variability maps onto the aPC neuronal responses. Using a linear mixed model (LME), we found a robust correlation between the initial binge feeding-induced aPC suppression and subsequent food consumption on each recording session (Figure 5L). Suppression was always quantified during the onset of a binge bout within the first 4 s after initiation. Our model, therefore, quantifies suppression independent of feeding bout duration. In keeping with the previously demonstrated results under variable palatability and metabolic state conditions, GABAergic OT responses also mirrored the aPC responses for different satiation levels. We observed a robust positive correlation between the overall initial binge feeding-induced OT activation and subsequent food consumption during each recording session (Figure 5M).

Optogenetic manipulation of aPC neurons bidirectionally modulates feeding

We have established the correlative relationship between feeding rate, suppression of olfactory flavor representation, palatability, satiation, and metabolic state. It remains unclear whether this effect directly impacts feeding behavior in the form of satiation. We, therefore, tested whether more substantial aPC suppression alone is sufficient to increase food consump-

tion and whether aPC activation during binge feeding reduces food consumption. We employed a closed-loop optogenetic paradigm to silence or activate aPC excitatory neurons at the initiation of binge feeding bouts (Figure 6A).^{23,56} We used channelrhodopsin (ChR2) to activate excitatory aPC neurons for excitation experiments. To suppress activity at the behavioral timescale (tens of seconds) typical of binge feeding bouts while minimizing the illumination period, we chose the highly light-sensitive targeting-enhanced mosquito homolog of the vertebrate encephalopsin eOPN3⁶² to provide long-lasting suppression of recurrent excitatory fibers in aPC (Figures 6B, S7A, and S7B). Mice consumed more food when we optogenetically suppressed aPC activity during feeding (Figures 6C, 6E, and 6F). This fits well with the observation that mice also eat more under conditions of hyposmia (Figures S4C–S4G). Optogenetically activating the aPC reduced food consumption. Light stimulation alone did not affect feeding behaviors in control mice transduced with adeno-associated viruses encoding tdTomato or GFP (Figures 6B, 6I, 6J, S7A, and S7B).

A reduction in satiation (the process of coming to feel full and stopping to eat during a meal) should result in more prolonged individual feeding bouts, indicating increased food liking. In contrast, an enhanced homeostatic drive to eat (wanting) usually increases the number of feeding bouts, implying reduced satiety (the feeling of fullness that lasts after a meal and prevents further eating).^{63,64} The optogenetic suppression of aPC activity prolonged the individual feeding bouts. Meanwhile, the number of feeding bouts remained similar, suggesting that optogenetic aPC suppression predominantly reduces satiation rather than satiety, aligning with enhanced food liking instead of wanting (Figures 6G and 6H). Additionally, ChR2 activation increased the number of feeding bouts (Figure 6K) while reducing individual feeding bout duration (Figure 6L). Our data show that binge feeding-induced aPC suppression is causally linked to feeding behavior, indicating a functional role of binge feeding-induced aPC suppression in modulating appetite by decreasing satiation and increasing food liking.

DISCUSSION

Here, we propose the aPC as a cortical hub for sensory satiation. The aPC must be connected to other brain regions' feeding centers to affect feeding behavior. A recent study reports disynaptic connections between the posterior PC (pPC) and feeding-related agouti-related peptide (AgRP)- and pro-opiomelanocortin (POMC)-expressing neurons in the hypothalamic nucleus arcuatus.⁶⁵ Considering the dense connectivity between aPC and pPC,⁶⁶ this indirect pathway may be related to sensory satiation via the aPC.

An alternative hypothesis regarding the link between the aPC and feeding is related to the effect of stress on feeding. Excitatory connections between the aPC and the lateral septum have recently been implicated in mediating behavioral disturbances that result from chronic social defeat stress. Generalized aPC suppression during the stress experience reduced behavioral stress symptoms.⁶⁷ Therefore, aPC suppression during binge feeding could enhance food liking by reducing stress levels during consumption. In humans, stress has been identified

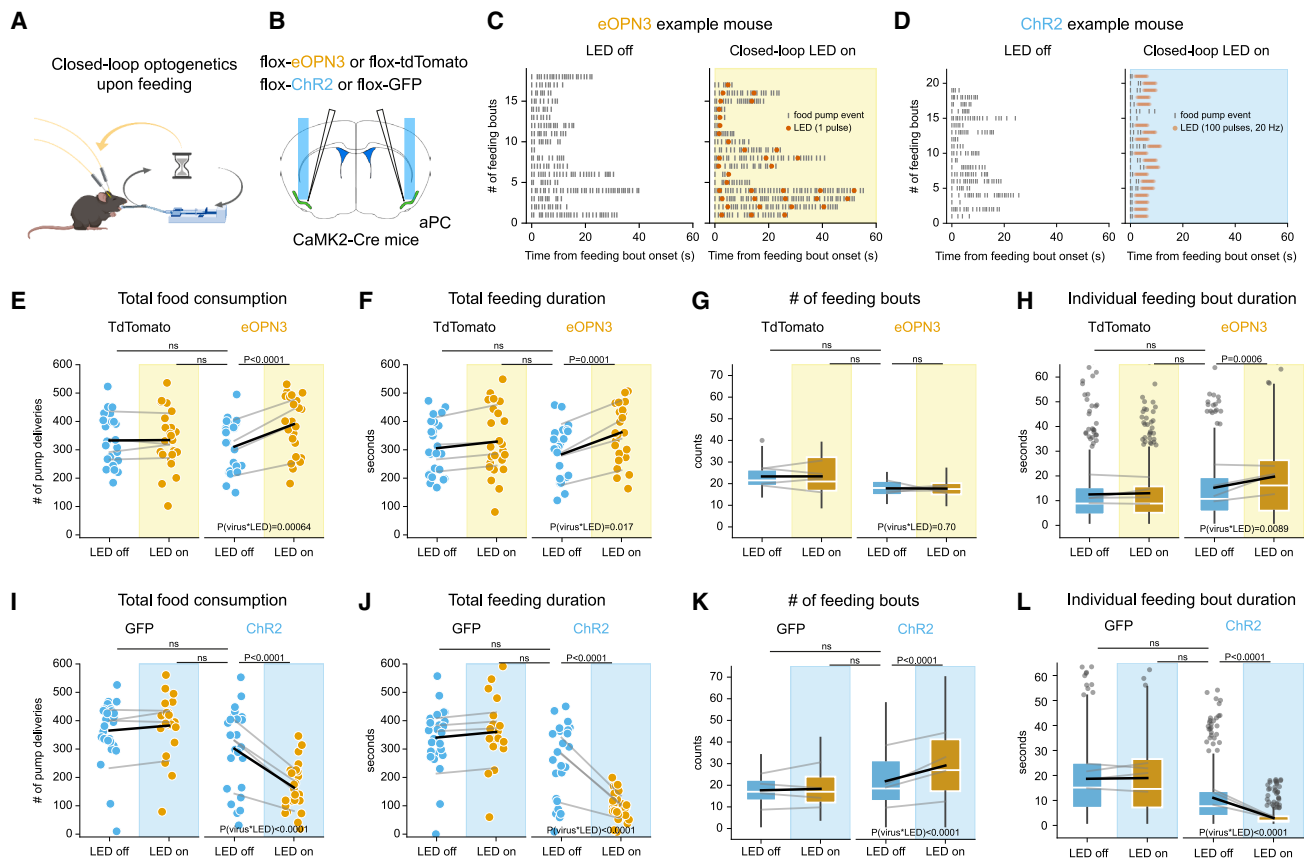


Figure 6. Optogenetically suppressing aPC neurons promotes feeding

(A) Schematics of closed-loop optogenetics experiment setup.

(B) Schematics of viral injection and optical fiber implants bilaterally in the aPC.

(C) Example feeding bouts in an eOPN3-expressing mouse without light stimulation (left) and with closed-loop light stimulation (right).

(D) Same as in (C) but with a ChR2-expressing mouse.

(E) Effects of light stimulation on total food consumption in tdTomato-expressing ($n = 6$ LED off sessions and 6 LED on sessions from 4 mice) and eOPN3-expressing ($n = 6$ LED off sessions and 6 LED on sessions from 4 mice) mice.

(F) Effects of light stimulation on total feeding duration in tdTomato- and eOPN3-expressing mice (n is the same as in E).

(G) Effects of light stimulation on the number of feeding bouts per session in tdTomato- and eOPN3-expressing mice (n is the same as in E).

(H) Effects of light stimulation on duration of individual feeding bouts in tdTomato-expressing ($n = 560$ for LED off sessions and $n = 561$ for LED on sessions from 4 mice) and eOPN3-expressing ($n = 428$ for LED off sessions and $n = 425$ for LED on sessions from 4 mice) mice.

(I–L) Same as in (E)–(H), but for GFP-expressing ($n = 6$ LED off sessions and 6 LED on sessions from 4 mice) and ChR2-expressing ($n = 6$ LED off sessions and 6 LED on sessions from 4 mice) mice (in L, GFP group: $n = 476$ for LED off sessions and $n = 385$ for LED on sessions, ChR2 group: $n = 526$ for LED off sessions and $n = 698$ for LED on sessions).

For (E)–(L), gray lines denote the data from the same mice, and the black line denotes the mean. For (H) and (L), the y scales were capped to emphasize data distribution, where a few extremely large data points were not shown. All data points were used for statistical analysis. For (E)–(L), p values of the interaction between LED states and viruses were calculated with an LME, and p values of the contrast analyses were estimated with emmeans and adjusted with Dunnett's method.

as a significant risk factor for binge eating.⁶⁸ It is tempting to speculate that the reduction in stress mediated by increases in feeding speed contributes to the pathogenesis of eating disorders related to binge eating.

We propose that GABAergic neurons in the OT are a potential source for mediating global inhibition in the aPC. This is supported by the OT's role as a center for value signaling.^{50,69–71} Neurons in the OT are mostly GABAergic.⁷² Although connectivity from the OT to the aPC was recently described,⁷³ another study labeled this pathway as negligible.⁵¹ Both studies selectively labeled outputs from D1- and D2-receptor-expressing

neurons. Here, we mapped axonal outputs from the larger population of all GABAergic neurons in the OT, including GABAergic neurons in the Islands of Calleja that were previously reported to project to the PC.^{74,75} However, we cannot rule out that the inhibition in the aPC may, for example, also be mediated by a polysynaptic pathway originating from the OT via the AON. A more detailed functional analysis of the OT circuits affecting the aPC during consumption will need to be explored in future studies. We also cannot exclude other inhibitory pathways, such as long-range GABAergic neurons from the diagonal band of Broca (DBB) in the basal forebrain,⁷⁶ which may also be involved in the

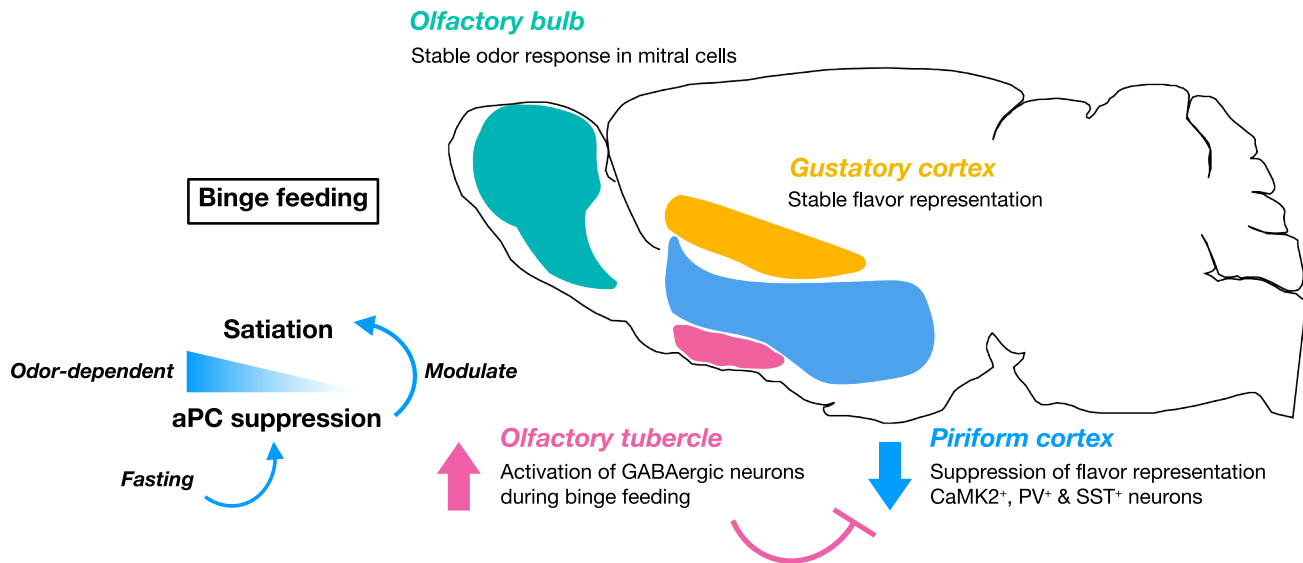


Figure 7. Graphic summary

In this study, we found a feeding-rate-dependent suppression of the olfactory flavor representation (Figures 1 and 3), whereas the gustatory flavor representation is not affected by the feeding rate (Figure 2). This binge feeding-induced suppression is mirrored in the OT GABAergic neurons (Figure 5), which functionally project to aPC (Figure 4). We further showed that optogenetically manipulating aPC excitatory neurons upon feeding bidirectionally modulates satiation (Figure 6).

binge feeding-induced aPC suppression. We did not examine the basal forebrain pathway because a recent study showed inhibited neuronal activity in the basal forebrain's DBB during feeding.⁷⁷

An important question is how the OT detects food value. Recently, the activation of dopaminergic neurons in the ventral tegmental area (VTA) has been shown to scale with the hedonic value of food to sustain palatable food consumption.² Although that study identified the nucleus accumbens as a target modulating feeding behavior, the OT could serve as a complementary dopaminergic target region modulating consumption at the sensory level. In the OT, dopamine amplifies direct olfactory inputs coming from the OB.⁷⁸ Dopaminergic signaling may also interact with other nutrient-sensing modalities projecting to the OT to encode food value. The OT is the only olfactory brain region that also receives viscerosensory inputs from the caudal nucleus tractus solitarius, a part of the dorsal vagal complex.^{79,80}

From an evolutionary perspective of food scarcity, overeating induced by suppression of sensory satiety would be beneficial. This is especially true when considering foods of a high hedonic value, usually associated with a high carbohydrate-to-fat ratio. These food items are designed to maximize the ratio between energy intake and satiety.⁸¹ Eating these high-value foods at a faster rate may further increase this ratio by reducing sensory satiation. Then, what would be the point of the more pronounced sensory representation during slow feeding that we describe here? A simple explanation could be that the artificial pause after receiving food in our slow feeding paradigm results in a reduced value signal from the OT, leading to less aPC suppression. However, slow feeding also occurs under conditions of food unfamiliarity. It has been shown that when mice experience unfamiliar flavors, the number of licks and lick clusters decreases,⁸² which

essentially describes a switch from binge to slow feeding. Slow feeding and the associated flavor representation in the aPC could be reserved for conditions of food unfamiliarity, where flavor encoding by the aPC may be a prerequisite for flavor learning. In line with this, strong PC activation has been demonstrated following the experience of novel food flavors.⁸³

However, in the surplus food environment human beings face today, an increased eating rate is correlated with overeating⁹ and obesity,¹⁰ while reducing the eating rate can effectively mitigate food consumption.^{3,7,84} Here, we demonstrate how feeding rate and olfactory flavor representation interact via sensory satiation to modulate appetite (Figure 7). We propose a mechanism of how palatable food items with a high hedonic value alter cortical flavor representation to reduce sensory satiation.

RESOURCE AVAILABILITY

Lead contact

Requests for further information, resources, and reagents should be directed to, and will be fulfilled by, the lead contact, Friedrich W. Jochenning (friedrich.jochenning@charite.de).

Materials availability

This study did not generate new unique reagents.

Data and code availability

Source data for plotting individual figure panels can be found on a GitHub repository (https://github.com/hung-lo/BingeFeeding_2023). Processed data can be found on the Zenodo data repository (<https://zenodo.org/records/15824561>). Raw imaging data will be available upon request due to the large file size (~2–3 TB). Code for plotting individual figure panels can be found on a GitHub repository (https://github.com/hung-lo/BingeFeeding_2023). An example code for data processing and analysis can be found on the GitHub repository (https://github.com/hung-lo/BingeFeeding_2023). Code for the

functional connectivity can be found on the GitHub repository (<https://github.com/KelschLAB/BingeEating>).

ACKNOWLEDGMENTS

We thank Susanne Rieckmann, Monika Dopatka, Anny Kretschmer, Katja Czeselsky, and Celina Ernst for their excellent technical assistance; Daniel Parthier for his inputs on statistical analysis; Yen-Chung Chen for his inputs on programming; Melissa Long from the Charité Animal Behavioral Phenotyping Facility, Charité Advanced Medical BIOimaging Core Facility, and Charité Viral Core Facility for their assistance; James Poulet and David Oswald for their feedback on the manuscript; Robin Blazing and Kevin Franks for sharing *in vivo* optical fiber implantation protocols; and Andreas Klaus for his input at the early stage of this study. Some figures were created using BioRender.com. We thank Chi-Chieh Lee for her contribution to the graphic abstract. H.L. is supported by a PhD fellowship from the Einstein Center for Neurosciences Berlin and the Taiwanese Government Scholarship to study abroad. F.W.J. is funded by the Deutsche Forschungsgemeinschaft (DFG) (project number 458236353 [hedonic eating] and project numbers 520617944 and 520223756 – SPP2411) (LOOPs). B.R.R. is supported by the DFG (project 327654276 – SFB1315 and project 273915538 – SPP1926). D.S. is supported by the DFG (project 184695641 – SFB 958, project 327654276 – SFB 1315, project 415914819 – FOR 3004, and project 431572356, the German Excellence Strategy EXC-2049-390688087, NeuroCure), by the European Research Council (ERC) under the European Union's Horizon 2020 research and innovation program (BrainPlay grant agreement no. 810580), and by the Federal Ministry of Education and Research (BMBF, SmartAge – project 01GQ1420B). E.R. is supported by #NEXTGENERATIONEU (NGEU) and funded by the Ministry of University and Research (MUR), National Recovery and Resilience Plan (NRRP), project MNESYS (PE0000006), a multiscale integrated approach to the study of the nervous system in health and disease (DN. 1553 11.10.2022). W.K. is supported by the DFG (KE1661/9-1).

AUTHOR CONTRIBUTIONS

Conceptualization, H.L., D.S., and F.W.J.; methodology, A.S., F.W.J., K.S., M.R., Y.W., M.L.S.T., B.J., M.E.L., W.C.R., E.R., and W.K.; investigation, H.L., F.W.J., M.L.S.T., L.F., L.M.V., A.K., A.H., and W.C.R.; validation, A.S., H.L., L.F., L.M.V., B.R.R., and F.W.J.; formal analysis, H.L., F.W.J., and W.C.R.; data curation, H.L., F.W.J., and W.K.; writing – original draft, H.L. and F.W.J.; writing – review & editing, D.S., B.R.R., M.R., B.J., K.S., M.L.S.T., M.E.L., L.F., M.R., L.M.V., Y.W., W.C.R., E.R., and W.K.; visualization, H.L. and W.C.R.; funding acquisition, F.W.J. and D.S.; resources, M.E.L., B.J., M.R., Y.W., D.S., and B.R.R.; project administration, A.S., F.W.J., and D.S.; and supervision, F.W.J., D.S., M.E.L., B.R.R., E.R., and W.K.

DECLARATION OF INTERESTS

Y.W. owns PhenoSys equity.

DECLARATION OF GENERATIVE AI AND AI-ASSISTED TECHNOLOGIES IN THE WRITING PROCESS

During the preparation of this work, the authors used Grammarly AI in order to polish manuscript text. After using this tool or service, the authors reviewed and edited the content as needed and take full responsibility for the content of the publication.

STAR★METHODS

Detailed methods are provided in the online version of this paper and include the following:

- [KEY RESOURCES TABLE](#)
- [EXPERIMENTAL MODEL AND STUDY PARTICIPANT DETAILS](#)
 - Mice
- [METHOD DETAILS](#)

- Liquid food delivery system
- Surgery procedures: Stereotactic injection
- Coordinates for viral injection and GRIN lens/prism implantation
- Surgery procedures: GRIN lens implantation
- Surgery procedures: Cranial window for olfactory bulb imaging
- *In vivo* Ca²⁺ imaging: Habituation
- *In vivo* Ca²⁺ imaging: *In vivo* miniscope imaging
- *In vivo* Ca²⁺ imaging: *In vivo* three-photon imaging
- Triton X-100 application
- Buried food test
- Closed-loop optogenetics
- Imaging processing
- *In vitro* electrophysiology
- Histology and imaging
- Serial two-photon tomography
- [QUANTIFICATION AND STATISTICAL ANALYSIS](#)
 - Data analysis, statistics, and plotting
 - Data synchronization
 - Binge feeding bout detection and slow feeding processing
 - Area under the receiver operating characteristics curve (auROC)
 - Effect size calculation
 - *q* values calculation
 - Linear mixed models
 - Functional interaction

SUPPLEMENTAL INFORMATION

Supplemental information can be found online at <https://doi.org/10.1016/j.neuron.2025.07.020>.

Received: November 30, 2023

Revised: May 13, 2025

Accepted: July 17, 2025

REFERENCES

1. Sternson, S.M., and Eiselt, A.-K. (2017). Three pillars for the neural control of appetite. *Annu. Rev. Physiol.* 79, 401–423. <https://doi.org/10.1146/annurev-physiol-021115-104948>.
2. Zhu, Z., Gong, R., Rodriguez, V., Quach, K.T., Chen, X., and Sternson, S.M. (2025). Hedonic eating is controlled by dopamine neurons that oppose GLP-1R satiety. *Science* 387, eadt0773. <https://doi.org/10.1126/science.adt0773>.
3. Scisco, J.L., Muth, E.R., Dong, Y., and Hoover, A.W. (2011). Slowing bite-rate reduces energy intake: an application of the bite counter device. *J. Am. Diet. Assoc.* 111, 1231–1235. <https://doi.org/10.1016/j.jada.2011.05.005>.
4. Andrade, A.M., Greene, G.W., and Melanson, K.J. (2008). Eating slowly led to decreases in energy intake within meals in healthy women. *J. Am. Diet. Assoc.* 108, 1186–1191. <https://doi.org/10.1016/j.jada.2008.04.026>.
5. Bolhuis, D.P., Lakemond, C.M.M., de Wijk, R.A., Luning, P.A., and de Graaf, C. (2013). Consumption with large sip sizes increases food intake and leads to underestimation of the amount consumed. *PLoS One* 8, e53288. <https://doi.org/10.1371/journal.pone.0053288>.
6. Teo, P.S., van Dam, R.M., and Forde, C.G. (2020). Combined Impact of a Faster Self-Reported Eating Rate and Higher Dietary Energy Intake Rate on Energy Intake and Adiposity. *Nutrients* 12, 3264. <https://doi.org/10.3390/nu12113264>.
7. Hurst, Y., and Fukuda, H. (2018). Effects of changes in eating speed on obesity in patients with diabetes: a secondary analysis of longitudinal health check-up data. *BMJ Open* 8, e019589. <https://doi.org/10.1136/bmjopen-2017-019589>.

8. Bolhuis, D.P., Forde, C.G., Cheng, Y., Xu, H., Martin, N., and de Graaf, C. (2014). Slow food: sustained impact of harder foods on the reduction in energy intake over the course of the day. *PLoS One* 9, e93370. <https://doi.org/10.1371/journal.pone.0093370>.
9. Hall, K.D., Ayuketah, A., Brychta, R., Cai, H., Cassimatis, T., Chen, K.Y., Chung, S.T., Costa, E., Courville, A., Darcey, V., et al. (2019). Ultra-Processed Diets Cause Excess Calorie Intake and Weight Gain: An Inpatient Randomized Controlled Trial of Ad Libitum Food Intake. *Cell Metab.* 30, 67–77.e3. <https://doi.org/10.1016/j.cmet.2019.05.020>.
10. Ohkuma, T., Hirakawa, Y., Nakamura, U., Kiyohara, Y., Kitazono, T., and Ninomiya, T. (2015). Association between eating rate and obesity: a systematic review and meta-analysis. *Int. J. Obes.* 39, 1589–1596. <https://doi.org/10.1038/ijo.2015.96>.
11. Ferriday, D., Bosworth, M.L., Godinot, N., Martin, N., Forde, C.G., Van Den Heuvel, E., Appleton, S.L., Mercer Moss, F.J., Rogers, P.J., and Brunstrom, J.M. (2016). Variation in the oral processing of everyday meals is associated with fullness and meal size; A potential nudge to reduce energy intake? *Nutrients* 8, 315. <https://doi.org/10.3390/nu8050315>.
12. Janani, R., Tan, V.W.K., Goh, A.T., Choy, M.J.Y., Lim, A.J., Teo, P.S., Stieger, M., and Forde, C.G. (2022). Independent and combined impact of texture manipulation on oral processing behaviours among faster and slower eaters. *Food Funct.* 13, 9340–9354. <https://doi.org/10.1039/d2fo00485b>.
13. Slyper, A. (2021). Oral Processing, Satiation and Obesity: Overview and Hypotheses. *Diabetes Metab. Syndr. Obes.* 14, 3399–3415. <https://doi.org/10.2147/DMSO.S314379>.
14. Samakidou, G.E., Koliaki, C.C., Liberopoulos, E.N., and Katsilambros, N. L. (2023). Non-Classical Aspects of Obesity Pathogenesis and Their Relative Clinical Importance for Obesity Treatment. *Healthcare (Basel)* 11, 1310. <https://doi.org/10.3390/healthcare11091310>.
15. Grove, J.C.R., Gray, L.A., La Santa Medina, N., Sivakumar, N., Ahn, J.S., Corpuz, T.V., Berke, J.D., Kreitzer, A.C., and Knight, Z.A. (2022). Dopamine subsystems that track internal states. *Nature* 608, 374–380. <https://doi.org/10.1038/s41586-022-04954-0>.
16. Chen, Y., Lin, Y.-C., Kuo, T.-W., and Knight, Z.A. (2015). Sensory detection of food rapidly modulates arcuate feeding circuits. *Cell* 160, 829–841. <https://doi.org/10.1016/j.cell.2015.01.033>.
17. Mandelblat-Cerf, Y., Ramesh, R.N., Burgess, C.R., Patella, P., Yang, Z., Lowell, B.B., and Andermann, M.L. (2015). Arcuate hypothalamic AgRP and putative POMC neurons show opposite changes in spiking across multiple timescales. *eLife* 4, e07122. <https://doi.org/10.7554/eLife.07122>.
18. Cecil, J.E., Francis, J., and Read, N.W. (1999). Comparison of the effects of a high-fat and high-carbohydrate soup delivered orally and intragastrically on gastric emptying, appetite, and eating behaviour. *Physiol. Behav.* 67, 299–306. [https://doi.org/10.1016/s0031-9384\(99\)00069-4](https://doi.org/10.1016/s0031-9384(99)00069-4).
19. Betley, J.N., Xu, S., Cao, Z.F.H., Gong, R., Magnus, C.J., Yu, Y., and Sternson, S.M. (2015). Neurons for hunger and thirst transmit a negative-valence teaching signal. *Nature* 521, 180–185. <https://doi.org/10.1038/nature14416>.
20. Cecil, J.E., Francis, J., and Read, N.W. (1998). Relative contributions of intestinal, gastric, oro-sensory influences and information to changes in appetite induced by the same liquid meal. *Appetite* 31, 377–390. <https://doi.org/10.1006/appe.1998.0177>.
21. Berkun, M.M., Kessen, M.L., and Miller, N.E. (1952). Hunger-reducing effects of food by stomach fistula versus food by mouth measured by a consummatory response. *J. Comp. Physiol. Psychol.* 45, 550–554. <https://doi.org/10.1037/h0061931>.
22. Stratton, R.J., and Elia, M. (1999). The effects of enteral tube feeding and parenteral nutrition on appetite sensations and food intake in health and disease. *Clin. Nutr.* 18, 63–70. [https://doi.org/10.1016/s0261-5614\(99\)80053-3](https://doi.org/10.1016/s0261-5614(99)80053-3).
23. Ly, T., Oh, J.Y., Sivakumar, N., Shehata, S., La Santa Medina, N., Huang, H., Liu, Z., Fang, W., Barnes, C., Dundar, N., et al. (2023). Sequential appetite suppression by oral and visceral feedback to the brainstem. *Nature* 624, 130–137. <https://doi.org/10.1038/s41586-023-06758-2>.
24. Aitken, T.J., Liu, Z., Ly, T., Shehata, S., Sivakumar, N., La Santa Medina, N., Gray, L.A., Zhang, J., Dundar, N., Barnes, C., et al. (2024). Negative feedback control of hypothalamic feeding circuits by the taste of food. *Neuron* 112, 3354–3370.e5. <https://doi.org/10.1016/j.neuron.2024.07.017>.
25. Small, D.M. (2012). Flavor is in the brain. *Physiol. Behav.* 107, 540–552. <https://doi.org/10.1016/j.physbeh.2012.04.011>.
26. Elliott, V.E., and Maier, J.X. (2020). Multisensory interactions underlying flavor consumption in rats: the role of experience and unisensory component liking. *Chem. Senses* 45, 27–35. <https://doi.org/10.1093/chemse/bjz067>.
27. Blazing, R.M., and Franks, K.M. (2020). Odor coding in piriform cortex: mechanistic insights into distributed coding. *Curr. Opin. Neurobiol.* 64, 96–102. <https://doi.org/10.1016/j.conb.2020.03.001>.
28. Bolding, K.A., and Franks, K.M. (2018). Recurrent cortical circuits implement concentration-invariant odor coding. *Science* 361, 1088. <https://doi.org/10.1126/science.aat6904>.
29. Choi, G.B., Stettler, D.D., Kallman, B.R., Bhaskar, S.T., Fleischmann, A., and Axel, R. (2011). Driving opposing behaviors with ensembles of piriform neurons. *Cell* 146, 1004–1015. <https://doi.org/10.1016/j.cell.2011.07.041>.
30. Shepherd, G.M. (2006). Smell images and the flavour system in the human brain. *Nature* 444, 316–321. <https://doi.org/10.1038/nature05405>.
31. Maier, J.X., Blankenship, M.L., Li, J.X., and Katz, D.B. (2015). A Multisensory Network for Olfactory Processing. *Curr. Biol.* 25, 2642–2650. <https://doi.org/10.1016/j.cub.2015.08.060>.
32. Niv, Y., Daw, N.D., Joel, D., and Dayan, P. (2007). Tonic dopamine: opportunity costs and the control of response vigor. *Psychopharmacology* 191, 507–520. <https://doi.org/10.1007/s00213-006-0502-4>.
33. Tantirigama, M.L.S., Huang, H.H.-Y., and Bekkers, J.M. (2017). Spontaneous activity in the piriform cortex extends the dynamic range of cortical odor coding. *Proc. Natl. Acad. Sci. USA* 114, 2407–2412. <https://doi.org/10.1073/pnas.1620939114>.
34. Roland, B., Deneux, T., Franks, K.M., Bathellier, B., and Fleischmann, A. (2017). Odor identity coding by distributed ensembles of neurons in the mouse olfactory cortex. *eLife* 6, e26337. <https://doi.org/10.7554/eLife.26337>.
35. Miura, K., Mainen, Z.F., and Uchida, N. (2012). Odor representations in olfactory cortex: distributed rate coding and decorrelated population activity. *Neuron* 74, 1087–1098. <https://doi.org/10.1016/j.neuron.2012.04.021>.
36. Stettler, D.D., and Axel, R. (2009). Representations of Odor in the Piriform Cortex. *Neuron* 64, 292.
37. Wilson, D.A., and Sullivan, R.M. (2011). Cortical processing of odor objects. *Neuron* 72, 506–519. <https://doi.org/10.1016/j.neuron.2011.10.027>.
38. Bolding, K.A., and Franks, K.M. (2017). Complementary codes for odor identity and intensity in olfactory cortex. *eLife* 6, e22630. <https://doi.org/10.7554/eLife.22630>.
39. Berners-Lee, A., Shtrahman, E., Grimaud, J., and Murthy, V.N. (2023). Experience-dependent evolution of odor mixture representations in piriform cortex. *PLoS Biol.* 21, e3002086. <https://doi.org/10.1371/journal.pbio.3002086>.
40. Frank, T., Mönig, N.R., Satou, C., Higashijima, S.-I., and Friedrich, R.W. (2019). Associative conditioning remaps odor representations and modifies inhibition in a higher olfactory brain area. *Nat. Neurosci.* 22, 1844–1856. <https://doi.org/10.1038/s41593-019-0495-z>.
41. Bekkers, J.M., and Suzuki, N. (2013). Neurons and circuits for odor processing in the piriform cortex. *Trends Neurosci.* 36, 429–438. <https://doi.org/10.1016/j.tins.2013.04.005>.

42. Cummings, D.M., Emge, D.K., Small, S.L., and Margolis, F.L. (2000). Pattern of olfactory bulb innervation returns after recovery from reversible peripheral deafferentation. *J. Comp. Neurol.* **421**, 362–373. [https://doi.org/10.1002/\(SICI\)1096-9861\(20000605\)421:3<362::AID-CNE5>3.0.CO;2-8](https://doi.org/10.1002/(SICI)1096-9861(20000605)421:3<362::AID-CNE5>3.0.CO;2-8).
43. Large, A.M., Vogler, N.W., Mielo, S., and Oswald, A.-M.M. (2016). Balanced feedforward inhibition and dominant recurrent inhibition in olfactory cortex. *Proc. Natl. Acad. Sci. USA* **113**, 2276–2281. <https://doi.org/10.1073/pnas.1519295113>.
44. Ren, J., Friedmann, D., Xiong, J., Liu, C.D., Ferguson, B.R., Weerakkody, T., DeLoach, K.E., Ran, C., Pun, A., Sun, Y., et al. (2018). Anatomically Defined and Functionally Distinct Dorsal Raphe Serotonin Sub-systems. *Cell* **175**, 472–487.e20. <https://doi.org/10.1016/j.cell.2018.07.043>.
45. Li, Y., Zhong, W., Wang, D., Feng, Q., Liu, Z., Zhou, J., Jia, C., Hu, F., Zeng, J., Guo, Q., et al. (2016). Serotonin neurons in the dorsal raphe nucleus encode reward signals. *Nat. Commun.* **7**, 10503. <https://doi.org/10.1038/ncomms10503>.
46. Lottem, E., Lörincz, M.L., and Mainen, Z.F. (2016). Optogenetic Activation of Dorsal Raphe Serotonin Neurons Rapidly Inhibits Spontaneous But Not Odor-Evoked Activity in Olfactory Cortex. *J. Neurosci.* **36**, 7–18. <https://doi.org/10.1523/JNEUROSCI.3008-15.2016>.
47. Gadziola, M.A., and Wesson, D.W. (2016). The Neural Representation of Goal-Directed Actions and Outcomes in the Ventral Striatum's Olfactory Tubercle. *J. Neurosci.* **36**, 548–560. <https://doi.org/10.1523/JNEUROSCI.3328-15.2016>.
48. Winkelmeier, L., Filosa, C., Hartig, R., Scheller, M., Sack, M., Reinwald, J. R., Becker, R., Wolf, D., Gerchen, M.F., Sartorius, A., et al. (2022). Striatal hub of dynamic and stabilized prediction coding in forebrain networks for olfactory reinforcement learning. *Nat. Commun.* **13**, 3305. <https://doi.org/10.1038/s41467-022-30978-1>.
49. Fitzgerald, B.J., Richardson, K., and Wesson, D.W. (2014). Olfactory tubercle stimulation alters odor preference behavior and recruits forebrain reward and motivational centers. *Front. Behav. Neurosci.* **8**, 81. <https://doi.org/10.3389/fnbeh.2014.00081>.
50. Zhang, Z., Liu, Q., Wen, P., Zhang, J., Rao, X., Zhou, Z., Zhang, H., He, X., Li, J., Zhou, Z., et al. (2017). Activation of the dopaminergic pathway from VTA to the medial olfactory tubercle generates odor-preference and reward. *eLife* **6**, e25423. <https://doi.org/10.7554/eLife.25423>.
51. Lee, D., Liu, L., and Root, C.M. (2024). Transformation of valence signaling in a mouse striatopallidal circuit. *eLife* **12**, RP90976. <https://doi.org/10.7554/eLife.90976>.
52. Feng, Q., An, S., Wang, R., Lin, R., Li, A., Gong, H., and Luo, M. (2021). Whole-brain reconstruction of neurons in the ventral pallidum reveals diverse projection patterns. *Front. Neuroanat.* **15**, 801354. <https://doi.org/10.3389/fnana.2021.801354>.
53. Root, D.H., Melendez, R.I., Zaborszky, L., and Napier, T.C. (2015). The ventral pallidum: Subregion-specific functional anatomy and roles in motivated behaviors. *Prog. Neurobiol.* **130**, 29–70. <https://doi.org/10.1016/j.pneurobio.2015.03.005>.
54. Veuthy, T.L., Derosier, K., Kondapavulur, S., and Ganguly, K. (2020). Single-trial cross-area neural population dynamics during long-term skill learning. *Nat. Commun.* **11**, 4057. <https://doi.org/10.1038/s41467-020-17902-1>.
55. Smedo, J.D., Jasper, A.I., Zandvakili, A., Krishna, A., Aschner, A., Machens, C.K., Kohn, A., and Yu, B.M. (2022). Feedforward and feedback interactions between visual cortical areas use different population activity patterns. *Nat. Commun.* **13**, 1099. <https://doi.org/10.1038/s41467-022-28552-w>.
56. Gong, R., Xu, S., Hermundstad, A., Yu, Y., and Sternson, S.M. (2020). Hindbrain Double-Negative Feedback Mediates Palatability-Guided Food and Water Consumption. *Cell* **182**, 1589–1605.e22. <https://doi.org/10.1016/j.cell.2020.07.031>.
57. Soria-Gómez, E., Bellocchio, L., Reguero, L., Lepousez, G., Martin, C., Bendahmane, M., Ruehle, S., Remmers, F., Desprez, T., Matias, I., et al. (2014). The endocannabinoid system controls food intake via olfactory processes. *Nat. Neurosci.* **17**, 407–415. <https://doi.org/10.1038/nn.3647>.
58. Aimé, P., Duchamp-Viret, P., Chaput, M.A., Savigner, A., Mahfouz, M., and Julliard, A.K. (2007). Fasting increases and satiation decreases olfactory detection for a neutral odor in rats. *Behav. Brain Res.* **179**, 258–264. <https://doi.org/10.1016/j.bbr.2007.02.012>.
59. Freeman, W.J. (1960). Correlation of electrical activity of prepyriform cortex and behavior in cat. *J. Neurophysiol.* **23**, 111–131. <https://doi.org/10.1152/jn.1960.23.2.111>.
60. Prud'homme, M.J., Lacroix, M.C., Badonnel, K., Gougis, S., Baly, C., Salesses, R., and Caillol, M. (2009). Nutritional status modulates behavioural and olfactory bulb Fos responses to isoamyl acetate or food odour in rats: roles of orexins and leptin. *Neuroscience* **162**, 1287–1298. <https://doi.org/10.1016/j.neuroscience.2009.05.043>.
61. Albrecht, J., Schreder, T., Kleemann, A.M., Schöpf, V., Kopietz, R., Anzinger, A., Demmel, M., Linn, J., Kettenmann, B., and Wiesmann, M. (2009). Olfactory detection thresholds and pleasantness of a food-related and a non-food odour in hunger and satiety. *Rhinology* **47**, 160–165.
62. Mahn, M., Saraf-Sinik, I., Patil, P., Pulin, M., Bitton, E., Karalis, N., Bruentgens, F., Palgi, S., Gat, A., Dine, J., et al. (2021). Efficient optogenetic silencing of neurotransmitter release with a mosquito rhodopsin. *Neuron* **109**, 1621–1635.e8. <https://doi.org/10.1016/j.neuron.2021.03.013>.
63. Dwyer, D.M. (2012). EPS Prize Lecture. Licking and liking: the assessment of hedonic responses in rodents. *Q. J. Exp. Psychol.* **65**, 371–394. <https://doi.org/10.1080/17470218.2011.652969>.
64. Kim, K.S., Park, J.S., Hwang, E., Park, M.J., Shin, H.Y., Lee, Y.H., Kim, K. M., Gautron, L., Godschall, E., Portillo, B., et al. (2024). GLP-1 increases preingestive satiation via hypothalamic circuits in mice and humans. *Science* **385**, 438–446. <https://doi.org/10.1126/science.adj2537>.
65. Kuang, D., Hanchate, N.K., Lee, C.-Y., Heck, A., Ye, X., Erdenebileg, M., and Buck, L.B. (2023). Olfactory and neuropeptide inputs to appetite neurons in the arcuate nucleus. Preprint at bioRxiv. <https://doi.org/10.1101/2023.02.28.530282>.
66. Hagiwara, A., Pal, S.K., Sato, T.F., Wienisch, M., and Murthy, V.N. (2012). Optophysiological analysis of associational circuits in the olfactory cortex. *Front. Neural Circuits* **6**, 18. <https://doi.org/10.3389/fncir.2012.00018>.
67. Okuda, Y., Li, D., Maruyama, Y., Sonobe, H., Mano, T., Tainaka, K., Shinohara, R., and Furuyashiki, T. (2024). The activation of the piriform cortex to lateral septum pathway during chronic social defeat stress is crucial for the induction of behavioral disturbance in mice. *Neuropsychopharmacology* **50**, 828–840.
68. Lim, M.C., Parsons, S., Goglio, A., and Fox, E. (2021). Anxiety, stress, and binge eating tendencies in adolescence: a prospective approach. *J. Eat. Disord.* **9**, 94. <https://doi.org/10.1186/s40337-021-00444-2>.
69. Gadziola, M.A., Stetzk, L.A., Wright, K.N., Milton, A.J., Arakawa, K., Del Mar Cortijo, M., and Wesson, D.W. (2020). A Neural System that Represents the Association of Odors with Rewarded Outcomes and Promotes Behavioral Engagement. *Cell Rep.* **32**, 107919. <https://doi.org/10.1016/j.celrep.2020.107919>.
70. Oettl, L.-L., Scheller, M., Filosa, C., Wieland, S., Haag, F., Loeb, C., Durstewitz, D., Shusterman, R., Russo, E., and Kelsch, W. (2020). Phasic dopamine reinforces distinct striatal stimulus encoding in the olfactory tubercle driving dopaminergic reward prediction. *Nat. Commun.* **11**, 3460. <https://doi.org/10.1038/s41467-020-17257-7>.
71. Millman, D.J., and Murthy, V.N. (2020). Rapid Learning of Odor-Value Association in the Olfactory Striatum. *J. Neurosci.* **40**, 4335–4347. <https://doi.org/10.1523/JNEUROSCI.2604-19.2020>.
72. Xiong, A., and Wesson, D.W. (2016). Illustrated Review of the Ventral Striatum's Olfactory Tubercle. *Chem. Senses* **41**, 549–555. <https://doi.org/10.1093/chemse/bjw069>.
73. Zhang, Z., Zhang, H., Wen, P., Zhu, X., Wang, L., Liu, Q., Wang, J., He, X., Wang, H., and Xu, F. (2017). Whole-Brain Mapping of the Inputs and

- Outputs of the Medial Part of the Olfactory Tubercle. *Front. Neural Circuits* 11, 52. <https://doi.org/10.3389/fncir.2017.00052>.
74. Fallon, J.H., Riley, J.N., Sipe, J.C., and Moore, R.Y. (1978). The islands of Calleja: organization and connections. *J. Comp. Neurol.* 181, 375–395. <https://doi.org/10.1002/cne.901810209>.
75. Fallon, J.H. (1983). The islands of Calleja complex of rat basal forebrain II: connections of medium and large sized cells. *Brain Res. Bull.* 10, 775–793. [https://doi.org/10.1016/0361-9230\(83\)90210-1](https://doi.org/10.1016/0361-9230(83)90210-1).
76. Hook, C., and Puche, A.C. (2023). Bulbar projecting subcortical GABAergic neurons send collateral branches extensively and selectively to primary olfactory cortical regions. *J. Comp. Neurol.* 531, 451–460. <https://doi.org/10.1002/cne.25434>.
77. Cassidy, R.M., Lu, Y., Jere, M., Tian, J.-B., Xu, Y., Mangieri, L.R., Felix-Okoroji, B., Selever, J., Xu, Y., Arenkiel, B.R., et al. (2019). A lateral hypothalamus to basal forebrain neurocircuit promotes feeding by suppressing responses to anxiogenic environmental cues. *Sci. Adv.* 5, eaav1640. <https://doi.org/10.1126/sciadv.aav1640>.
78. Igarashi, K.M., Ieki, N., An, M., Yamaguchi, Y., Nagayama, S., Kobayakawa, K., Kobayakawa, R., Tanifuji, M., Sakano, H., Chen, W. R., et al. (2012). Parallel mitral and tufted cell pathways route distinct odor information to different targets in the olfactory cortex. *J. Neurosci.* 32, 7970–7985. <https://doi.org/10.1523/JNEUROSCI.0154-12.2012>.
79. Guevara-Aguilar, R., Donatti-Albarran, O.A., Solano-Flores, L.P., and Wayner, M.J. (1987). Nucleus of the tractus solitarius projections to the olfactory tubercle: an HRP study. *Brain Res. Bull.* 18, 673–675. [https://doi.org/10.1016/0361-9230\(87\)90138-9](https://doi.org/10.1016/0361-9230(87)90138-9).
80. Randolph, A.B., Zheng, H., and Rinaman, L. (2024). Populations of hind-brain glucagon-like peptide 1 (GLP1) neurons that innervate the hypothalamic PVH, thalamic PVT, or limbic forebrain BST have axon collaterals that reach all central regions innervated by GLP1 neurons. *J. Neurosci.* 44, e2063232024. <https://doi.org/10.1523/JNEUROSCI.2063-23.2024>.
81. Rogers, P.J., Vural, Y., Berridge-Burley, N., Butcher, C., Cawley, E., Gao, Z., Sutcliffe, A., Tinker, L., Zeng, X., Flynn, A.N., et al. (2024). Evidence that carbohydrate-to-fat ratio and taste, but not energy density or NOVA level of processing, are determinants of food liking and food reward. *Appetite* 193, 107124. <https://doi.org/10.1016/j.appet.2023.107124>.
82. Austen, J.M., Strickland, J.A., and Sanderson, D.J. (2016). Memory-dependent effects on palatability in mice. *Physiol. Behav.* 167, 92–99. <https://doi.org/10.1016/j.physbeh.2016.09.001>.
83. Zimmerman, C.A., Bolkan, S.S., Pan-Vazquez, A., Wu, B., Keppler, E.F., Meares-Garcia, J.B., Guthman, E.M., Fetcho, R.N., McMannon, B., Lee, J., et al. (2025). A neural mechanism for learning from delayed post-ingestive feedback. *Nature* 642, 700–709. <https://doi.org/10.1038/s41586-025-08828-z>.
84. Bolhuis, D.P., Lakemond, C.M.M., de Wijk, R.A., Luning, P.A., and de Graaf, C. (2014). Both a higher number of sips and a longer oral transit time reduce ad libitum intake. *Food Qual. Prefer.* 32, 234–240. <https://doi.org/10.1016/j.foodqual.2013.10.001>.
85. Chen, T.-W., Wardill, T.J., Sun, Y., Pulver, S.R., Renninger, S.L., Baohan, A., Schreiter, E.R., Kerr, R.A., Orger, M.B., Jayaraman, V., et al. (2013). Ultrasensitive fluorescent proteins for imaging neuronal activity. *Nature* 499, 295–300. <https://doi.org/10.1038/nature12354>.
86. Dana, H., Sun, Y., Mohar, B., Hulse, B.K., Kerlin, A.M., Hasseman, J.P., Tsegaye, G., Tsang, A., Wong, A., Patel, R., et al. (2019). High-performance calcium sensors for imaging activity in neuronal populations and microcompartments. *Nat. Methods* 16, 649–657. <https://doi.org/10.1038/s41592-019-0435-6>.
87. Schneider, C.A., Rasband, W.S., and Eliceiri, K.W. (2012). NIH Image to ImageJ: 25 years of image analysis. *Nat. Methods* 9, 671–675. <https://doi.org/10.1038/nmeth.2089>.
88. Schindelin, J., Arganda-Carreras, I., Frise, E., Kaynig, V., Longair, M., Pietzsch, T., Preibisch, S., Rueden, C., Saalfeld, S., Schmid, B., et al. (2012). Fiji: an open-source platform for biological-image analysis. *Nat. Methods* 9, 676–682. <https://doi.org/10.1038/nmeth.2019>.
89. Harris, C.R., Millman, K.J., van der Walt, S.J., Gommers, R., Virtanen, P., Cournapeau, D., Wieser, E., Taylor, J., Berg, S., Smith, N.J., et al. (2020). Array programming with NumPy. *Nature* 585, 357–362. <https://doi.org/10.1038/s41586-020-2649-2>.
90. Hunter, J.D. (2007). Matplotlib: A 2D Graphics Environment. *Comput. Sci. Eng.* 9, 90–95. <https://doi.org/10.1109/MCSE.2007.55>.
91. Waskom, M. (2021). seaborn: statistical data visualization. *J. Open Source Softw.* 6, 3021. <https://doi.org/10.21105/joss.03021>.
92. Pedregosa, F., Varoquaux, G., Gramfort, A., Michel, V., Thirion, B., Grisel, O., Blondel, M., Müller, A., Nothman, J., Louppe, G., et al. (2012). Scikit-learn: Machine Learning in Python. Preprint at arXiv. <https://doi.org/10.5555/1953048.2078195>.
93. Virtanen, P., Gommers, R., Oliphant, T.E., Haberland, M., Reddy, T., Cournapeau, D., Burovski, E., Peterson, P., Weckesser, W., Bright, J., et al. (2020). SciPy 1.0: fundamental algorithms for scientific computing in Python. *Nat. Methods* 17, 261–272. <https://doi.org/10.1038/s41592-019-0686-2>.
94. Ho, J., Tumkaya, T., Aryal, S., Choi, H., and Claridge-Chang, A. (2019). Moving beyond P values: data analysis with estimation graphics. *Nat. Methods* 16, 565–566. <https://doi.org/10.1038/s41592-019-0470-3>.
95. Giovannucci, A., Friedrich, J., Gunn, P., Kalfon, J., Brown, B.L., Koay, S. A., Taxis, J., Najafi, F., Gauthier, J.L., Zhou, P., et al. (2019). CalmAn an open source tool for scalable calcium imaging data analysis. *eLife* 8, e38173. <https://doi.org/10.7554/eLife.38173>.
96. Lopes, G., Bonacchi, N., Frazão, J., Neto, J.P., Atallah, B.V., Soares, S., Moreira, L., Matias, S., Itskov, P.M., Correia, P.A., et al. (2015). Bonsai: an event-based framework for processing and controlling data streams. *Front. Neuroinform.* 9, 7. <https://doi.org/10.3389/fninf.2015.00007>.
97. Viejo, G., Levenstein, D., Skromne Carrasco, S., Mehrotra, D., Mahallati, S., Vite, G.R., Denny, H., Sjulson, L., Battaglia, F.P., and Peyrache, A. (2023). Pynapple, a toolbox for data analysis in neuroscience. *eLife* 12, RP85786. <https://doi.org/10.7554/eLife.85786>.
98. Pachitariu, M., Stringer, C., Schröder, S., Dipoppa, M., Rossi, L.F., Carandini, M., and Harris, K.D. (2016). Suite2p: beyond 10,000 neurons with standard two-photon microscopy. Preprint at bioRxiv. <https://doi.org/10.1101/061507>.
99. Tyson, A.L., Vélez-Fort, M., Rousseau, C.V., Cossell, L., Tsitoura, C., Lenzi, S.C., Obenhaus, H.A., Claudi, F., Branco, T., and Margrie, T.W. (2022). Accurate determination of marker location within whole-brain microscopy images. *Sci. Rep.* 12, 867. <https://doi.org/10.1038/s41598-021-04676-9>.
100. Claudi, F., Petrucco, L., Tyson, A., Branco, T., Margrie, T., and Portuguese, R. (2020). BrainGlobe Atlas API: a common interface for neuroanatomical atlases. *J. Open Source Softw.* 5, 2668. <https://doi.org/10.21105/joss.02668>.
101. Bates, D., Mächler, M., Bolker, B., and Walker, S. (2015). Fitting linear mixed-effects models Using lme4. *J. Stat. Softw.* 67, 1–48. <https://doi.org/10.18637/jss.v067.i01>.
102. Ryu, B., Nagappan, S., Santos-Valencia, F., Lee, P., Rodriguez, E., Lackie, M., Takatoh, J., and Franks, K.M. (2021). Chronic loss of inhibition in piriform cortex following brief, daily optogenetic stimulation. *Cell Rep.* 35, 109001. <https://doi.org/10.1016/j.celrep.2021.109001>.
103. Zhou, P., Resendez, S.L., Rodriguez-Romaguera, J., Jimenez, J.C., Neufeld, S.Q., Giovannucci, A., Friedrich, J., Pnevmatikakis, E.A., Stuber, G.D., Hen, R., et al. (2018). Efficient and accurate extraction of in vivo calcium signals from microendoscopic video data. *eLife* 7, e28728. <https://doi.org/10.7554/eLife.28728>.
104. Paxinos, G., and Franklin, K.B.J. (2019). *Paxinos and Franklin's the Mouse Brain in Stereotaxic Coordinates* (Academic Press).
105. Ragan, T., Kadiri, L.R., Venkataraju, K.U., Bahlmann, K., Sutun, J., Taranda, J., Arganda-Carreras, I., Kim, Y., Seung, H.S., and Osten, P.

- (2012). Serial two-photon tomography for automated ex vivo mouse brain imaging. *Nat. Methods* 9, 255–258. <https://doi.org/10.1038/nmeth.1854>.
106. Wang, Q., Ding, S.-L., Li, Y., Royall, J., Feng, D., Lesnar, P., Graddis, N., Naeemi, M., Facer, B., Ho, A., et al. (2020). The Allen Mouse Brain Common Coordinate Framework: A 3D reference atlas. *Cell* 181, 936–953.e20. <https://doi.org/10.1016/j.cell.2020.04.007>.
107. Haase, R. (2023). Napari tutorial. Zenodo. <https://doi.org/10.5281/ZENODO.10207321>.
108. Ichihara, Y.G., Okabe, M., Iga, K., Tanaka, Y., Musha, K., and Ito, K. (2008). Color universal design: the selection of four easily distinguishable colors for all color vision types. In *Proceedings of SPIE - The International Society for Optical Engineering*, pp. 206–213. <https://doi.org/10.1117/12.765420>.
109. Botta, P., Fushiki, A., Vicente, A.M., Hammond, L.A., Mosberger, A.C., Gerfen, C.R., Peterka, D., and Costa, R.M. (2020). An Amygdala Circuit Mediates Experience-Dependent Momentary Arrests during Exploration. *Cell* 183, 605–619.e22. <https://doi.org/10.1016/j.cell.2020.09.023>.
110. Cohen, J.Y., Haesler, S., Vong, L., Lowell, B.B., and Uchida, N. (2012). Neuron-type-specific signals for reward and punishment in the ventral tegmental area. *Nature* 482, 85–88. <https://doi.org/10.1038/nature10754>.

STAR★METHODS

KEY RESOURCES TABLE

REAGENT or RESOURCE	SOURCE	IDENTIFIER
Bacterial and virus strains		
AAV1: pAAV.Syn.Flex.GCaMP6f.WPRE.SV40	Chen et al. ⁸⁵	Addgene AAV1; 100833-AAV1; RRID: Addgene_100833
AAV8: pAAV-Syn-iCre-RFP	Plasmid and virus were made in the Charité viral core (BA-48c)	Charité viral core id: BA-48c
AAV1: pGP-AAV-syn-jGCaMP7s-WPRE	Dana et al. ⁸⁶	Addgene AAV1; 104487-AAV1; RRID: Addgene_104487
AAV9: pAAV-hSyn-Flex-OPN3-mScarlet-minWPRE	Plasmid and virus were made in the Charité viral core (BA-575b)	N/A
AAV9: hSyn-flox-tdTomato	Plasmid and virus were made in the Charité viral core (BA-234a)	N/A
AAV5: EF1a-double floxed-hChR2(H134R)-EYFP-WPRE-HGHpA	Plasmid was a gift from Karl Deisseroth (Addgene plasmid # 20298); virus was made in the Charité viral core (BA-180c)	Addgene plasmid; 20298; RRID: Addgene_20298
AAV1: CAG-flex-GFP	Virus was made in the Charité viral core (BA-02)	N/A
AAV9: CaMK2-iCre-WPRE	Virus was made in the Charité viral core (BA-696a)	Charité viral core id: BA-696a
Deposited data		
Processed data	This paper	Zenodo: https://zenodo.org/records/15824561
Experimental models: Organisms/strains		
C57BL/6N	Charité Central Animal Facility	N/A
Ai93D; Ai93(TITL-GCaMP6f)-D	JAX	JAX: 024103; RRID: IMSR_JAX:024103
Rosa-tTA	JAX	JAX: 011008; RRID: IMSR_JAX:011008
Ai148D; Ai148(TIT2L-GC6f-ICL-tTA2)-D	JAX	JAX: 030328; RRID: IMSR_JAX:030328
CaMKII-CreT29	JAX	JAX: 005359; RRID: IMSR_JAX:005359
PV-Cre	JAX	JAX: 008069; RRID: IMSR_JAX:008069
SST-Cre	JAX	JAX: 013044; RRID: IMSR_JAX:013044
VGAT-Cre	JAX	JAX: 017535; RRID: IMSR_JAX:017535
Software and algorithms		
Fiji/ImageJ	Schneider et al. ⁸⁷ and Schindelin et al. ⁸⁸	RRID: SCR_002285; Version: 2.14.0/1.54f
Python	Python Software Foundation	RRID: SCR_008394; Version: 3.9
Numpy	Harris et al. ⁸⁹	NumPy, RRID: SCR_008633; Version: 1.21.5
Matplotlib	Hunter ⁹⁰	Matplotlib, RRID: SCR_008624; Version: 3.5.1
Seaborn	Waskom ⁹¹	seaborn, RRID: SCR_018132; Version: 0.12.2
Scikit-learn	Pedregosa et al. ⁹²	scikit-learn, RRID: SCR_002577; Version: 1.1.1
Statsmodels	Seabold et al. https://github.com/statsmodels/statsmodels/blob/main/CITATION.cff	statsmodel, RRID: SCR_016074; Version: 0.13.5
Scipy	Virtanen et al. ⁹³	SciPy, RRID: SCR_008058; Version: 1.8.0
Dabest	Ho et al. ⁹⁴	Version: 0.3.1
CNMFe/CalmAn	Giovannucci et al. ⁹⁵	Calcium Imaging data Analysis, RRID: SCR_021533; Git forked version: https://github.com/flatironinstitute/CalmAn.git@7dc5b42ab06c6a6b86ff1520dfc5b2334f335a78

(Continued on next page)

Continued

REAGENT or RESOURCE	SOURCE	IDENTIFIER
Inscopix CNMFe wrapper		https://github.com/inscopix/isx-cnmfe-wrapper@v1.2
Inscopix CNMFe	Inscopix	https://github.com/inscopix/inscopix-cnmfe
Inscopix python API	Inscopix	N/A
Inscopix Data Processing Software v1.31, v1.6.0, v1.8.0	Inscopix	N/A
Inscopix Data Acquisition System	Inscopix	Version: 1.3.1
Bonsai	Lopes et al. ⁹⁶	Bonsai, RRID: SCR_021512; Version: 2.4.0
FlyCapture2		Version: 2.11.3.425
Pyanple	Viejo et al. ⁹⁷	Version: 0.3.1
LSMAQ		https://github.com/danionella/lismaq
Suite2P	Pachitariu et al. ⁹⁸	https://github.com/MouseLand/suite2p ; RRID: SCR_016434
Sticht		https://github.com/SainsburyWellcomeCentre/Sticht
BrainReg	Tyson et al. ⁹⁹	https://github.com/brainglobe/brainreg
Cellfinder	Claudi et al. ¹⁰⁰	https://github.com/brainglobe/cellfinder
BakingTray		https://github.com/SainsburyWellcomeCentre/BakingTray
R	R Core Team (2021). R: A language and environment for statistical computing. R Foundation for Statistical Computing, Vienna, Austria. https://www.R-project.org/ .	Version: 4.2.2; RRID: SCR_001905
Rstudio	Posit team (2025). RStudio: Integrated Development Environment for R. Posit Software, PBC, Boston, MA. (http://www.posit.co/)	Version: 2022.12.0+353; RRID:SCR_000432
Ime4	Bates et al. ¹⁰¹	Version: 1.1.31;RRID: SCR_015654
Illustrator	Adobe	v27.4.1, 2023; RRID: SCR_010279
MATLAB	MathWorks	Version: R2020a

EXPERIMENTAL MODEL AND STUDY PARTICIPANT DETAILS**Mice**

Animals were kept at the animal facility of Charité, under a regular 12/12 h light-dark cycle. All procedures involving animal experiments were approved by the local authorities and ethics committee (LaGeSo Berlin, license numbers G0278/16, G0313/16, and G0156/20). To image excitatory neurons in aPC, we cross-bred Ai93D mice, Rosa-tTA mice, and CaMK2-Cre mice to obtain Ai93D; Rosa-tTA; CaMK2-Cre mice that express GCaMP6f in excitatory cells. To prevent early expression of GCaMP during development, the breeding pairs and offspring were fed with doxycycline-containing food to suppress the expression of GCaMP6f until weaning. A subset of aPC excitatory neurons imaging mice ($n = 3$ mice, used in [Figures 1F](#), [1G](#), [5E](#), and [5J](#)) was performed in Ai148D mice with viral injection of CaMK2-Cre virus. Due to suboptimal GCaMP6f expression in the GC in the abovementioned transgenic mice, we injected the adeno-associated virus (AAV) carrying hSyn-Cre in the GC of Ai148D mice to express GCaMP6f in the GC. To image GABAergic neurons in the aPC, we performed viral injection of Cre-dependent GCaMP6f in PV-Cre or SST-Cre mice. To image serotonin and dopamine levels in the aPC, wildtype C57BL/6N mice were injected with AAVs containing iSeroSnFR or dLight 1.3b. For mapping the axonal projection of OT GABAergic neurons, we injected Cre-dependent eOPN3-mScarlet virus in the VGAT-Cre mice and imaged with serial two-photon tomography (see [STAR Methods](#)). To image GABAergic neurons in the OT, we performed viral injection of Cre-dependent GCaMP6f in the VGAT-Cre mice. For optogenetic activation of aPC neurons, CaMK2-Cre mice were bilaterally injected with Cre-dependent hCHR2(H134R)-EYFP virus or Cre-dependent GFP virus for controls. For optogenetic inhibition of aPC neuron axons, CaMK2-Cre mice were bilaterally injected with Cre-dependent eOPN3-mScarlet virus or a Cre-dependent tdTomato virus for controls. Both sexes of mice were used in the study as we did not observe significant

difference in sex differences (see statistical summary for the optogenetic experiments). All experiments, including Ca^{2+} imaging and optogenetics, are performed between 9 a.m. to 6 p.m. under regular light.

METHOD DETAILS

Liquid food delivery system

To reduce stress, we performed experiments inside the animals' home cages. Cages were modified so that we could protrude the motorized lick spout (Phenosys, Berlin, Germany) into the cage. After a 5-min baseline period, motorized lick spouts were presented in the cage and primed for liquid delivery for 2 min with 1 min intervals between presentations. During these intervals, the spouts were retracted. To control the feeding rate, we implemented different time-out periods for the delivery pump: 4 s for the slow feeding mode and 0.4 s for the binge feeding mode. Over 30 min, mice had access to the spout for a total of 14 min, with a pseudorandom order of 2-min-long periods of slow or binge feeding. For olfactory isolation, we presented the lick spout inside a glass tube with an opening for animals to reach the spout. Air suction from the glass tube limited olfactory responses to the food odor to the time period just before and while mice interacted with the lick spout. Lick spouts were equipped with piezo sensors to register each licking. Licks triggered a 400-ms activation of electrical pumps, which resulted in the delivery of one droplet ($\sim 1.8 \mu\text{L}$) of strawberry or chocolate-flavored Ensure (Abbott Laboratories), sucrose or water. During slow feeding, we provided water and Ensure at a ratio of 7 to 3. Four slow-feeding rounds and three binge-feeding rounds were interchanged in a pseudorandom order. Mice were *ad libitum* fed before the experiments, with a maximal period of up to 4 h of pre-experiment food deprivation during the light cycle. Fasting was performed once a week for 20–22 h before starting the experiment.

Surgery procedures: Stereotactic injection

Mice were anesthetized by inhalation anesthesia with isoflurane (induction: 4–5%, then 1–2% with oxygen, flow rate 0.5–1 L/min). Mice were local anesthetized with Lidocaine (1–2%) subcutaneous injection preincision. A craniotomy was performed over the stereotactically determined target regions (see the “Coordinates for viral injection and GRIN lens/prism implantation” table) using a semi-automatic Neurostar stereotactic apparatus (Neurostar, Tübingen, Germany). The virus (0.4 to 1 μL) was injected using a 10 μL -Hamilton syringe. Postoperative pain was prevented by Carprofen (5 mg/kg) subcutaneous injection right before surgery and in the first 3 days after surgery. After the surgery, the animals recovered for at least 2 weeks. In some experiments, implantation of the prism or the optic stimulation fiber was performed right after viral injection.

Coordinates for viral injection and GRIN lens/prism implantation

Brain regions	Coordinates (AP/ML/DV) (mm)	Notes
aPC	0.32/-3.1/5.4 0.32/-2.7/5.5 (10° coronal angle)	For viral injection For implantation, we used the bottom right corner of the Prism of the GRIN lens.
GC	0.26/-3.6/4.0 0.26/-3.0/4.1 (10° coronal angle)	For viral injection For implantation, we used the bottom right corner of the Prism of the GRIN lens.
OB	4.3-4.6 / ± 0.6 / 0.3	For viral injection
OT	0.75/-1.7/6.0 0.75/-1.3/6.0 (no angle)	For viral injection For implantation, we used the bottom right corner of the Prism of the GRIN lens.

Surgery procedures: GRIN lens implantation

Mice (>P50) were anesthetized for the procedure by inhalation anesthesia with isoflurane (induction: 4–5%, then 1–2% with oxygen, flow rate 0.5–1 L/min). Mice were local anesthetized with Lidocaine (1–2%) subcutaneous injection preincision. The anesthetized animals were fixed in the stereotact (Neurostar, Tübingen), and a craniotomy was performed over the stereotactically determined target region (see the “Coordinates for viral injection and GRIN lens/prism implantation” table). The side length of the quadratic craniotomy was slightly larger than the side length of the prism base. The insertion tract was paved by aspiration of brain tissue until ~ 1 mm above the image plane of the microscope. Aspiration was performed through a thin needle (23G, sharp end) linked to a vacuum pump, and the procedure was performed twice to ensure sufficient aspiration of brain tissues. Any small hemorrhagic foci that occurred were staunched by Gelfoam. After removal of the Gelfoam and any pending blood clots, insertion of the microendoscopic lens (GRIN lens attached with a Prism [1 mm diameter, ~ 9.1 or ~ 4.3 mm long, Inscopix]) to the desired image plane was performed at a rate of 100 $\mu\text{m}/\text{min}$ according to the coordinates in the “Coordinates for viral injection and GRIN lens/prism implantation” table.

With the aid of an adhesive (VetBond, 3M, or TRUGLUE, TRUSETAL) and dental cement (Super-Bond C&B, SUNMEDICAL), microendoscopes with attached baseplates (Inscopix) were fixed to the skull, and the optical surface was protected from contamination by a plastic cap (Inscopix baseplate cover). Postoperative pain was prevented by Carprofen (5 mg/kg) subcutaneous injection right before surgery and in the first 3 days after surgery. In a subset of mice, we did not use microendoscopes with attached baseplates. In this case, the slightly protruding microendoscope was fixed to the skull with adhesive and dental cement, and the optical surface was protected from contamination using a silicone cap. In these mice, a baseplate was fixed in the desired optical plane above the protruding lens in a surgery performed at least 4 weeks after the lens implant.

Surgery procedures: Cranial window for olfactory bulb imaging

Mice (C57BL/6, <P40) were anesthetized with isoflurane (induction: 4–5%, then 1–2% with oxygen, flow rate 0.5–1 l/min). Mice were local anesthetized with Lidocaine (1–2%) subcutaneous injection preincision. After the scalp and periosteum were removed, a 3 mm craniotomy was made over the two bulb hemispheres. An injection micropipette (tip diameter, 10–20 μm) was filled with AAV1.Syn.jGCaMP7s.WPRE virus solution (Penn Vector Core), and 100 nl was injected 50 nl/min at a depth of 300 μm in either bulb hemisphere (see “Coordinates for viral injection and GRIN lens/prism implantation” table for coordinates). After injection, a semi-circular <3mm stack of two glass coverslips, glued to each other using optical adhesive, was fitted into the craniotomy and sealed with cyanoacrylate glue and dental cement. Finally, a light-weight head-post was fixed on the skull over the left hemisphere with light-curing adhesives (RelyX, 3M) and dental cement (Ortho-Jet, Lang Dental). Postoperative pain was prevented by Buprenorphine (0.05–0.1 mg/kg) and Carprofen (5 mg/kg) subcutaneous injection right before surgery and then Carprofen (5 mg/kg) in the first days after surgery. Head-fixed three-photon imaging experiments began 3 weeks after the virus injection.

In vivo Ca^{2+} imaging: Habituation

For freely-moving recordings, before starting the combined behavioral and imaging sessions using Ensure and water, mice were habituated to the lick spout delivery with 10% sucrose solution. Mice had to reach a criterion of 25 sucrose deliveries in slow feeding mode in a 45-min habituation session before the actual measurements began. Mice were further habituated with additional air suction around the lick spout and dummy scope mounting once they had learned to drink from the lick spout. The habituation period usually lasted \sim 3 weeks.

For head-fixed recordings, the habituation of mice to head-fixation began at least 5 days before imaging. On the first day, the animal was head-fixed on a running wheel for 5 min and then gradually increased each day until it was calm for 1 h. At least 1 day before imaging, a lick spout with Ensure/water within easy reach for licking was introduced.

In vivo Ca^{2+} imaging: In vivo miniscope imaging

The miniaturized microscope (nVista miniscope, Inscopix, CA, USA) was mounted right before the imaging session started without anesthesia. Before the recording started, mice were allowed to explore the home cage for 3–5 min. After a baseline period of 5 min, the lick spout protruded according to the protocol described above. For each mouse, the imaging settings (LED intensity, gain, focus, etc.) were individually tuned to reach a similar level of brightness (mean values around 50–60 A.U. in fluorescence histogram function in Inscopix acquisition software). We recorded at 20 Hz with a single focal plane. Most imaging sessions were 4x spatially down-sampled during acquisition to save storage space. The behavioral system was linked with the Inscopix system using TTL pulses upon pump activation. We performed up to 25 imaging sessions per mouse across 5 weeks, and overnight food deprivation was performed once per week. We could stably record around 140 aPC excitatory neurons per imaging session (Figure S1K).

In vivo Ca^{2+} imaging: In vivo three-photon imaging

Imaging from head-fixed mice was performed with a home-built three-photon microscope. The laser (Opera-F, pumped by Monaco, Coherent) provided light pulses at 1300 nm wavelength and 1 MHz repetition rate for excitation of jGCaMP7s. The laser output passed a four-pass prism pulse compressor for dispersion compensation. Laser power was adjusted using a motorized half-wave plate and a polarizing beam splitter, and was below 20 mW under the objective. We used a Nikon 25x/1.1 objective and dual linear galvanometers at a frame rate of \sim 10 Hz. Image acquisition was synchronized with laser pulses and was controlled by LSMAQ (<https://github.com/danionella/lsmaq>). Time-series images (200 x 200 pixels) were recorded at depths of 200–300 μm below the pia at the mitral cell layer.

Triton X-100 application

Nasal lavage with 0.5% of Triton X-100 (in 0.1M PBS) can introduce temporal hyposmia in mice for up to 3 weeks.⁴² Mice were anesthetized with Ketamin (100 mg/kg), Xylazine (20 mg/kg) and Acepromazine (3 mg/kg) intraperitoneal injection. They received Caprofen (5 mg/kg) subcutaneous injection before and the day after the Triton X-100 (experimental group) or PBS (control group) applications. We applied 40 μL 0.5% Triton X-100 solution to each nostril with a gel-loading pipette tip that was advanced for 2–3 mm into the nostril. Triton solution was slowly applied with a micropump (Narishige, Japan) over several minutes on each side, with an interval of 5 min between the two nostrils. Foam building up at the opening of the nostrils was an indicator of a successful procedure. Throughout the procedure and until waking up from anesthesia, mice were kept on an inclined plane so that their nostrils were below their trachea and lungs in a heated chamber.

Buried food test

To test the efficacy of Triton-induced anosmia, we examined the ability of hyposmic mice to find a hidden food pellet located 1 cm deep in the bedding of the experimental cage. Mice were overnight food-deprived and habituated to the experimental cage for at least 5 min before the experiment started. After the food pellet was buried, mice were transferred into the experimental cage. The time to find the pellet was documented by the experimenter. The experiment was stopped if the mice did not find the pellet after 15 min. Control experiments were performed with mice that had undergone the same lavage procedure with 0.1M PBS nasal lavage. The buried food tests were repeated every week to monitor the mice's olfactory capability and ensure the mice remained hyposmic throughout our experiments.

Closed-loop optogenetics

Mice expressing ChR2/GFP or eOPN3/tdTomato in aPC excitatory neurons were anesthetized for the procedure by inhalation anesthesia with isoflurane (induction: 4-5%, then 1-2% with oxygen, flow rate 0.5-1 L/min). The anesthetized animals were fixed in the stereotact (Neurostar, Tübingen), and a craniotomy was performed over the stereotactically determined target region. Fiberoptic cannulas (200 μ m diameter, NA 0.66, length 5 mm, Doric lenses) were inserted bilaterally until reaching the target coordinates (Figure S7). The slightly protruding fiber with an attached zirconia sleeve for taking up the stimulation fiber patchcord was fixed to the skull with adhesive and dental cement, and the optical surface was protected from contamination using a plastic cap.

Before starting the combined behavioral and optogenetic stimulation sessions using Ensure, the mice were habituated to the lick spout delivery with 10% sucrose solution. Mice had to reach a criterion of 25 sucrose deliveries in binge feeding mode and needed to successfully trigger sham closed-loop stimulations in a 20-min habituation session before the actual measurements began. At the start of the experiment, we plugged a splitter branching patchcord (200 μ m diameter, NA 0.57, Doric) connected to a mono fiberoptic patchcord (480 μ m diameter, NA 0.63, Doric) onto the fiberoptic cannulas. Activating aPC neurons via ChR2 has been reported to trigger seizure-like events.¹⁰² To avoid this, we limited the blue light (470 nm, Doric) intensity at 0.5 mW or lower at the tip of the fibers, for which we did not observe seizure-like behaviors. The increased number of feeding bouts indicates that the mice were still motivated to visit the food source under closed-loop ChR2 activation. This suggests that our stimulation paradigm was not perceived as aversive. For activating eOPN3, white light from a Ce:YAG fiber light source (Doric) was delivered at an intensity of 8 mW at the tip of the fibers. For these experiments, mice were granted constant access to the lick spout in the binge feeding mode over a period of 60 min. Upon detection of a binge bout (3 pump deliveries with a maximum of a 1.5 s interdelivery interval), a train of 100 pulses at 20 Hz (for ChR2) or a single 500 ms light stimulus (for eOPN3) was delivered on "LED on" days. After detecting a binge bout with a subsequent light stimulus, there was a minimal refractory period of 10 s until a binge bout could initiate the next light stimulus. Everything was similar on "LED off" days, apart from not stimulating with light upon binge bout detection. LED on and off days were alternated for 12 subsequent days.

Imaging processing

Ca²⁺ movies obtained from miniscope recordings were first temporally downsampled to 10 Hz. We then cropped out regions in the field of view (FoV) where no active Ca²⁺ transients were visible. The same FoV cropping parameters were used throughout recordings from the same mice. Movies were then bandpassed with a spatial filter (low cutoff = 0.005, high cutoff = 0.500, Inscopix IDPS) and motion corrected (aligned to mean image or first frame, max_translation = 20, Inscopix IDPS). Ca²⁺ traces were extracted with CNMFe¹⁰³ with the following parameters (Cell diameter: 10 px, PNR: 10, except 20 for aPC GABAergic cells, Corr: 0.8). Ca²⁺ traces were manually curated with predefined selection criteria (peak amplitude >80 A.U., baseline drifts smaller than 20% of peak fluorescence, clear cell shape, locate outside blood vessels, minimal motion artifacts of given regions of interest).

Image stacks from 3P imaging were loaded into Suite2P⁹⁸ for motion correction, region-of-interest (ROI) segmentation, and trace extraction using the settings specified in the appended exemplary ops file. We used the 'mean img', 'correlation map', and 'max projection' views of Suite2P to manually check and sort somatic from non-somatic ROIs of mitral cells. The output from Suite2P was analyzed in Python: Detected neuropil signals were subtracted. Remaining frames with movement artifacts were then detected and excluded based on the presence of post-registration x- and y-shifts at each time point. A further criterion was the phase correlation of individual frames and the reference image below a threshold of 50% of the maximum peak of phase correlation in the respective stack. After that, $\Delta F/F$ values and Z scores were calculated.

In vitro electrophysiology

All experiments were conducted at 32-34°C. Axon Multiclamp 700B amplifier (Molecular Devices) was used for the electrophysiological recordings. We filtered the signals with 2 kHz and digitized the signal at a 20 kHz sampling rate (BNC-2090, National Instruments Corporation). We filled the glass pipettes (resistance 3-6 M Ω) with an intracellular solution (135 mM K-gluconate, 6 mM KCl, 10 mM HEPES, 0.2 mM EGTA, 2 mM MgCl₂, 2 mM Na-ATP, 0.5 mM Na-GTP, 5 mM phosphocreatine Na (pH 7.3), and 0.2% biocytine). We did not correct for liquid junction potential. In current clamp, we compensated the bridge balance. If a cell had a resting membrane potential above -60 mV or if the series resistance was larger than 30 M Ω , the cell was discarded. No holding current was applied for the dopamine modulation experiments. We patched layer 2b (superficial pyramidal) aPC neurons based on their morphology and location in the aPC. 10 μ M of dopamine was applied in the bath and incubated for 5 min before starting recording. For current injection

protocols, the injected current is tuned in the range of 80–150 pA to aim for triggering 3–5 action potentials for baseline conditions, and each current stimulation is repeated 6 times under both baseline and dopamine wash-in conditions.

Histology and imaging

Mice were anesthetized with Ketamine (100 mg/kg) and Xylazine (15 mg/kg) and perfused with 0.1M PBS and then 4% paraformaldehyde (PFA). Mice brains were harvested and stored in 4% PFA at 4°C overnight and transferred to 0.1M PBS for long-term storage. Brains were embedded in 4% agar-agar and sliced at 100–150 μm thickness with a vibratome. Brain slices were mounted on glass slides and were imaged by an epifluorescence microscope (Leica DMI8) or a confocal microscope (Leica SP5). Acquired images were then aligned to the mouse brain atlas¹⁰⁴ for registration of the location of GRIN lens-prism or fiber optic cannula implants.

Serial two-photon tomography

A subset of fixed mouse brains was sliced and imaged by serial 2P tomography, where whole forebrain structures can be imaged at cellular resolutions.¹⁰⁵ We modified a custom-made 2P microscope to operate with BakingTray (ScanImage & BakingTray, MATLAB, <https://bakingtray.mouse.vision/>). Obtained images were stitched (StitchIt, MATLAB) and reconstructed into 3D brain models. Accordingly, images in Figures 4B–4L are composite images stitched from distinct serially acquired tiles. Image stacks were then registered to the Allen mouse brain atlas (BrainReg, Python) and visualized with napari (Python).^{99,106,107} The whole-brain image in Figure 4B is gaussian filtered and enhanced in napari (Python) to emphasize the OT projecting regions.

QUANTIFICATION AND STATISTICAL ANALYSIS

Data analysis, statistics, and plotting

All data analysis was performed using customized scripts in Python, MATLAB, and R. Statistical analysis was performed in Python (Scipy, Numpy, Dabest), MATLAB, and R (Lmer). Individual statistical tests are listed under the respective figure legends, and all statistical details are listed in the statistical summary table (Table S1). Mean \pm standard error of the mean (SEM) or 95% confidence interval was used to report statistics in figures. A significance level of $p < 0.05$ is used for rejecting the null hypothesis. No statistical methods were used to predetermine sample size, randomization, nor was blinding applied. Given the sample size and symmetry of the data, we assumed approximate normality and applied parametric statistical tests. All statistical analyses were performed in Python, MATLAB, and R. Most figures were plotted in Python (matplotlib, seaborn) and MATLAB, and figure and font sizes were later modified in Illustrator (Adobe). We used the Okabe-Ito color palette¹⁰⁸ to increase the accessibility for common forms of color blindness.

Data synchronization

Ca²⁺ imaging data and behavioral data were synchronized by finding the time lag of maximum cross-correlation between pump events in digital values from the Phenosys behavioral protocol and the binarized pump-triggered TTL pulses recorded in the Inscopix system by Pynapple.cross_correlogram (Python).

Binge feeding bout detection and slow feeding processing

To detect binge feeding bouts, inter-pump intervals were calculated for each pump event, and only pump deliveries with intervals shorter than 2 s qualified as part of a feeding bout. Additionally, each feeding bout was required to include at least 3 pump deliveries. When analyzing slow feeding, neurons were aligned to individual deliveries, followed by a 4-s interval to the next delivery. Activity during binge feeding was aligned to the first delivery in a binge bout, followed by the first 4 s during which the animal activates the pump at 0.5 to 2 Hz.

Pump events in slow feeding mode were filtered out if no further lick event followed the initial lick event triggering pump activation. Initial motor artifacts from the movement of the lick spout were also removed from further analysis. Since binge feeding bouts were guaranteed to have subsequent lick events by design, the exclusion of pump events following no lick events was not applied to binge feeding pump events.

Area under the receiver operating characteristics curve (auROC)

We used auROC to classify neurons into different response classes to Ensure and water deliveries during slow feeding.^{109,110} In individual neurons, we compared the distribution of raw Ca²⁺ amplitudes during baseline activity (–1 to 0 s before pump activation) to the distribution of raw Ca²⁺ amplitudes in individual 100-ms bins across trials. To produce the bin-specific ROC curves, we moved the criterion from the minimal to the maximal Ca²⁺ response we found in the neuron's baseline activity distribution and the given 100-ms bin distribution. We then plotted the probability that Ca²⁺ signals in the given 100-ms bin distribution were larger than the criterion against the probability that the Ca²⁺ signals in the baseline distribution were larger than the criterion. The auROC for each bin was then calculated using the auc function (sklearn.metrics.auc), resulting in auROC values between 0–1, and 0.5 means not different from the baseline. The post-stimulus auROC values from each time bin were compared to the baseline auROC values. Significance was established if at least four consecutive post-stimulus bin values between 0–2 s were greater than 2 S.D. of the pre-stimulus baseline values (food-, sucrose-, or water-activated neurons).

Effect size calculation

To calculate the effect size of binge feeding-induced suppression in each neuron class, we performed a bootstrap-coupled estimation (DABEST, Python). To obtain the distribution of the mean difference between the two conditions, we resampled the mean Ca^{2+} activity of two conditions (e.g., slow feeding and binge feeding) 5000 times (bootstrapping distribution, represented as the violin plot). The distribution was then normalized by the pooled standard deviation of both conditions to convert it to Cohen's d using the `Dabest.cohens_d` (DABEST). p values were computed with the `Dabest.PermutationTest` (DABEST).

q values calculation

To estimate the differences between 2 neuronal time series along the time axis, we first calculated the p values of each time bin by performing the unpaired Student's t test (`scipy.stats.ttest_ind`). Then we applied false discovery rate correction (`statsmodels.stats.multitest.fdr correction`) to obtain the adjusted p values, which are the q values.

Linear mixed models

Linear mixed models were used to estimate contributions of predictors (e.g., level of excitation/suppression in neuronal activities upon feeding, or interaction of optogenetic actuators and light stimulation) to outcome (e.g., food consumption or feeding duration) while allowing different intercepts for individual mice (lmer, R). To calculate the contribution of a given predictor, we built a full model with all predictors and a reduced model that lacks the given predictor. We then compared these two models with the `anova` function (R) to calculate the p value of the given predictor. Representative models are structured as follows:

Full model

$$\text{Food.consumption} \sim 1 + \text{session} + \text{bodyweight} + \text{baseline.time} + \text{sex} + \text{virus} + \text{LED.state} + \text{virus} * \text{LED.state} + (1|\text{mouse.id})$$

Reduced model (without interaction of optogenetic actuator and LED state)

$$\text{Food.consumption} \sim 1 + \text{session} + \text{bodyweight} + \text{baseline.time} + \text{sex} + \text{virus} + \text{LED.state} + (1|\text{mouse.id})$$

Functional interaction

Dataset

We examined OT-aPC interactions on a dataset previously published in Winkelmeier et al.⁴⁸ The dataset is composed of $n_{\text{sessions}} = 67$ sessions from $n_{\text{mice}} = 11$ mice with simultaneously recorded units both in OT and aPC (Figures S6A and S6B). Mice were trained in a delay-conditioned task where conditioned odor stimuli (CS, 1 s) and a delay (1.7 s) were followed, or not, by the unconditioned water reward (US). Mice were exposed to three different CS with reward-outcome probabilities of 0%, 50%, and 100%, respectively. In each session, each of the three CS was presented in 50 trials (trial duration between 10 s and 12 s) in pseudorandomized order. The task shaped a value-encoding inhibitory response in the aPC throughout the delay and US.⁴⁸

Canonical correlation analysis (CCA)

CCA is a linear technique that allows for the identification of the subspace of shared covariance, between two sets of multivariate time series. In the population spaces of the OT and the aPC, CCA identifies axes, defined by sets of weights and referred to as canonical components, along which the projections of the two regions' activities exhibit maximal correlation, thereby identifying the respective subspaces of potential functional connectivity. Significance is assessed by determining whether the identified correlation reflects trial-to-trial variability (noise correlation) rather than just the shared modulation of the two regions to the task (signal correlation).

Here, CCA is used to identify the two axes along which the projections of OT and aPC activity, respectively, have maximal Pearson's correlation r (as such, r is always positive). We performed CCA in sliding windows of 2 s. First, we aligned the spiking activity with respect to CS onset and binned the spike counts in 100-ms bins. Then, we concatenated the bins within the 2-s windows from the 150 trials of the session. We then normalized the spike count of each unit separately by subtracting their mean and dividing by their standard deviation. To obtain a lagged canonical correlations, we shifted the 2-s window of one of the two regions by lags ranging from -25 ms to -275 ms in steps of 25 ms, and from -275 ms to -575 ms in steps of 50 ms (the results from the negative lagging of the OT are reported in the Figure 4, and those of the aPC in the Figure S6). The procedure was repeated by sliding the original 20-bin window in 100 ms steps over the trial duration (x axis in Figures 4P and 4Q; the computed statistics are reported as aligned to the center of the 20-bin window).

Statistical significance of the CCA

The resulting r was tested for statistical significance at the session level by a shuffle test, in which the order of the trials of one of the two regions is randomized within trial type (according to odor identity and reward delivery). The shuffle procedure is repeated 4,800 times, from which a distribution r_{shuffle} is obtained under the null hypothesis of independence between regions. In particular, by retaining the trial type in the shuffled distribution, $r > r_{\text{shuffle}}$ implies that the identified correlation goes beyond a shared mean response to the stimuli (signal correlation), but reflects trial-to-trial co-fluctuations of the two regions (noise correlation). At the session level, the p value of r is given by the fraction of r_{shuffle} larger than r . To evaluate the significance of r across sessions, we derived for each session a z value by subtracting from r the mean of r_{shuffle} and dividing by the standard deviation of r_{shuffle} . The resulting z -values were pooled

across the 67 sessions ($n_{mice} = 11$), and the overall significance was tested through a linear mixed effects model (LME) to account for the identity of the mice. The LME was computed using the function *fitlme* (Matlab R2020a) and the model equation $z \sim 1 + (1|Mouse)^{\prime}$. The result is an estimate with standard error, $\beta \pm \sigma_{\beta}$, and the associated t-statistic, $t = \beta/\sigma_{\beta}$, from which the p value is derived comparing to the t-distribution given the degrees of freedom ($DOF = n_{sessions} - 1 = 66$). In the window between 1.8 s and 2.1 s after CS onset with the activity of the OT lagged between -325 ms and -250 ms with respect to the aPC, the model estimates that r is $\beta = 1.2 \pm 0.2$ standard deviations above the mean of the shuffle distribution.

Sign of the correlation

To determine whether the identified co-modulation pattern between regions is predominantly correlational (excitation→excitation or inhibition→inhibition) or anti-correlational (excitation→inhibition or inhibition→excitation), we defined the quantity d :

$$d = \frac{\sum_i^{N_{aPC}} w_i^{aPC} \sum_j^{N_{Tu}} w_j^{Tu}}{\sum_i^{N_{aPC}} |w_i^{aPC}| \sum_j^{N_{Tu}} |w_j^{Tu}|}$$

with N_{aPC} and N_{Tu} the number of units samples in the session aPC and OT, respectively, and w the set of weights used to project the activity of the units in both regions along the respective axes identified by the CCA. To obtain an overall estimate of the nature of the interaction, we computed the mean across sessions of $d \cdot r$, giving more weight to sessions with high canonical correlation (as r is strictly positive, while z can be negative) (Figure 4Q).

Observing the communication subspace

To analyze the modulation by the CS of the activity in the communication subspace, we selected the sessions with significant $r > r_{shuffle}$ ($p < 0.05$) within the window from 1.8 s to 2.1 s after CS onset with the OT activity lagged between -250 ms and -325 ms (37 sessions, at least one per mouse, Figure S6A), and extracted the weights from the bin with the lowest p value in each session. The activity in the communication subspace is obtained by projecting the activity of the units with the weights found by the CCA.

We tested whether the different CS modulated the activity in the subspace of each region. Since reversing the direction of the canonical axis in both regions leaves their correlation unchanged and thus might randomly vary across sessions, we decided to quantify the activity in the communication subspace as absolute deviation from the baseline projection. To this aim, we built an LME (Matlab 2020a, function *fitlme*) with model formula $\Delta \sim 1 + CS + (Mouse) + (Mouse : Session)^{\prime}$ where Δ is the vector of absolute mean deviations from baseline for each trial type for each session. We then performed post-hoc comparisons between CS with the function *coefTest* on the output of *fitlme* to compare the effect sizes between pairs of CS types. The windows from which the activities were obtained are, with respect to CS onset: for baseline, -1.7 s to 0 s; and for the window of interest in aPC, 1 s to 2.7 s; and in OT, 0.725 s to 2.425 s.

To quantify firing rate modulation in both regions linked to the identified interaction, we calculated the weighted mean of each region's unit activity, using the absolute values of the corresponding CCA weights. For this analysis, CCA was applied directly to the raw unit activities without normalization. To test whether the regions had an excitatory or inhibitory response within the identified communication subspace, we estimated the deviation from baseline with an LME (Matlab 2020a, function *fitlme*) with model formula $\delta \sim 1 + (Mouse) + (Mouse : Session) + (Session : CS)^{\prime}$, where δ is the vector of the difference between the projected rates and the projected baseline for each trial. The windows from which the activities were obtained are again, with respect to CS onset: for baseline, -1.7 s to 0 s; and for the window of interest in aPC, 1 s to 2.7 s; and in OT, 0.725 s to 2.425 s. The model was estimated including only CS100 and CS50 trials. We tested whether δ was significantly different from 0.

Instantaneous firing rate

To estimate the instantaneous firing rate for the plots in Figures 4R and 4S, the spike times were convoluted with a half-Gaussian probability distribution function f :

$$f(t, \sigma) = \begin{cases} 0 & \text{if } t < 0 \\ \sqrt{\frac{2}{\pi}} \frac{1}{\sigma} e^{-\frac{1}{2}(\frac{t}{\sigma})^2} & \text{if } t \geq 0 \end{cases}$$

with $\sigma = 300$ ms. The convoluted data was sampled every 100 ms and scaled by a factor of 10 to reflect spikes per second (Hz). In Figure 4R, we plotted the mean across the significant 37 sessions of the absolute mean deviation from baseline (-1.7 s to 0 s) of the projected activity in the communication subspace for different trial types. In Figure 4S, we plotted the mean across the 37 sessions of the weighted mean of the instantaneous firing rate weighted with the CCA absolute weights. For this plot, CCA was applied directly to the raw unit activities without normalization.